HAL
open science

Organized growth of semiconducting one-dimensional nanostructures in vertical porous templates for the fabrication of field effect transistors

Emmanuel Lefeuvre

To cite this version:

Emmanuel Lefeuvre. Organized growth of semiconducting one-dimensional nanostructures in vertical porous templates for the fabrication of field effect transistors. Micro and nanotechnologies/Microelectronics. Ecole Polytechnique X, 2012. English. NNT : . pastel-01063869

HAL Id: pastel-01063869

https://pastel.hal.science/pastel-01063869v1

Submitted on 14 Sep 2014

HAL is a multi-disciplinary open access archive for the deposit and dissemination of scientific research documents, whether they are published or not. The documents may come from teaching and research institutions in France or abroad, or from public or private research centers.

L'archive ouverte pluridisciplinaire **HAL**, est destinée au dépôt et à la diffusion de documents scientifiques de niveau recherche, publiés ou non, émanant des établissements d'enseignement et de recherche français ou étrangers, des laboratoires publics ou privés.

Thèse

présentée pour obtenir le grade de

DOCTEUR DE L'ECOLE POLYTECHNIQUE

spécialité "Science des Matériaux"

par

Emmanuel LEFEUVRE

Organized growth of semiconducting one-dimensional nanostructures in vertical porous templates for the fabrication of field effect transistors

soutenue le 03/12/2012 devant le jury composé de :

Sylvie ROUSSET	Rapporteur
Rabah BOUKHERROUB	Rapporteur
Jérémy MALLET	Examinateur
Thierry BARON	Examinateur
Costel-Sorin COJOCARU	Examinateur
Marc CHATELET	Directeur de thèse

"When you have eliminated the impossible,
whatever remains, however improbable,
must be the truth"

Sir Arthur Conan Doyle - The Sign of the Four

Remerciements

Je souhaite avant tout remercier Bernard Drévillon, directeur du LPICM, qui m'a accueilli dans son laboratoire en m'accordant sa confiance pour ces quelques trois années et demi de thèse. Je le remercie aussi pour ses conseils d'orientation professionnelle.

Je remercie Didier Pribat, qui le premier a accepté mon arrivée dans son équipe en 2009, avant de laisser sa place quelques mois plus tard. Bien sûr je n'oublie pas notre rencontre à San Diego en 2010.

Merci aux personnes qui ont constitué mon jury de thèse et qui se sont déplacées pour assister à la soutenance: Thierry Baron, Jérémy Mallet, Rabah Boukherroub et Sylvie Rousset.

Je remercie chaleureusement mon directeur de thèse Marc Châtelet, pour son encadrement, ses conseils et ses corrections avisées dans mon manuscrit.

Costel-Sorin Cojocaru m'a toujours encouragé dans mes recherches, et notamment dans les moments les plus difficiles où il est important de trouver une source de motivation. Sa connaissance de la physique m'a été d'une grande aide pour comprendre les phénomènes que j'observais, et ses idées de piste de recherche ont relancé plus d'une fois ma motivation pendant cette thèse. Je le remercie aussi pour son attention et ses conseils quant à la poursuite de ma carrière.

Je remercie Bernd Marquardt, à qui j'ai repris le flambeau et qui m'a donné la première impulsion pour commencer cette thèse. Je salue la gentillesse et la patience dont il a fait preuve pour me former, pendant une phase de rédaction où le temps ne jouait pas en sa faveur. J'espère avoir dignement poursuivi son travail ici.

Je dois beaucoup à toutes les personnes qui m'ont aidé de près ou de loin à faire avancer mes recherches, notamment au bureau d'études avec Frédéric Farci, Jérôme Charliac, et Cyril Jadaud. Léo Caristan et Garry Rose ont toujours été disponibles et étonnamment rapides pour me sortir de situations qui me bloquaient techniquement, je salue donc ici leur efficacité et leur gentillesse. Je remercie également Eric Paillassa et Frédéric Liège pour leur support concernant le matériel informatique. Merci à Aurélien Gohier et Chang-Seok Lee pour leur aide avec le reacteur plasma, à Jean-Eric Bourrée pour son dévouement lors de la conférence HWCVD6 à laquelle j'ai pu participer, et un merci tout particulier à Jean-Luc Maurice et Zhan-Bing He pour le travail de qualité qu'ils ont bien voulu mener avec moi sur l'observation TEM de mes nano-fils. Le troisième chapitre de cette thèse s'en trouve considérablement renforcé. Je remercie également Waleed Moujahid pour le temps qu'il a consacré à tenter d'imprimer des électrodes sur mes échantillons, ainsi que Ki-Hwan, mon partenaire de PAA auprès de qui j'ai tant appris et dont l'ardeur au travail m'a si souvent tiré vers le haut. Je le remercie pour notre collaboration au sein de NanoMaDe, pour les conseils qu'il a pu me donner et les services qu'il m'a rendu.

Je ne peux pas omettre ces dames de l'administration, qui ont tant fait pour me faciliter la vie dans le labo. Je pense à Laurence Corbel, qui a jonglé avec tous mes contrats,

à Chantal Geneste, qui a géré toutes mes commandes (malgré mes petites erreurs), et à Carine Roger-Roulling, grâce à qui j'ai pu traverser l'Atlantique à deux reprises. Je les remercie très chaleureusement.

J'ai aussi eu l'occasion d'aller embêter des personnes extérieures au laboratoire avec mon travail, notamment à Thales (TRT) à Palaiseau et à l'Institut d'Electronique Fondamentale d'Orsay. A ce titre je remercie particulièrement Didier Thénot de TRT qui m'a formé aux techniques de gravure, aidé et conseillé dans ce domaine tout au long de ma thèse. Je salue aussi la gentillesse et la disponibilité de Martine Carbonnelle, qui m'a formé à la lithographie. Du côté de l'IEF, il a été particulièrement agréable d'échanger avec Nathalie Isac pour la gravure et José Palomo pour les dépôts. Je les remercie vivement, ainsi que Jean-René Coudevylle et Cédric Villebasse pour leurs formations en gravure et en nettoyage respectivement. Toutes ces dernières personnes m'ont beaucoup appris et je les tiens en partie responsable du succès de la fabrication de l'empilement poreux si délicat à réaliser.

J'en viens enfin à saluer et à remercier toutes les personnes dont l'importance pour moi n'a cessé de grandir au cours de ces années. Parmi elles Evgeny, qui a partagé mon bureau pendant deux ans et demi et qui m'a appris presque plus de choses sur la langue française que je lui ai moi-même appris. Ben, avec qui j'ai partagé beaucoup plus que notre passion commune pour les nano-fils, et que je remercie pour avoir été tant de fois mon complice le vendredi soir venu. Clément, qui n'était jamais à court d'idées pour me les changer, notamment grâce aux liens de ses collègues de bureau Gaël et Bat et aux moments passés rue du Faubourg du Temple. Je salue Romain, même si je suis secrètement jaloux de sa maîtrise du slackline, Guillaume, mon digne successeur au badminton, et Martin, dont le manuscrit sert toujours de modèle. Bien sur merci à Coralie. De Palaiseau à Boston, son amitié et nos longues discussions sont de très bons souvenirs. Enfin, merci à Maher pour sa sympathie et son humanité. Nous allons nous revoir souvent, si j'ai bien compris.

Je finis ces remerciements en pensant à ma famille et à mes amis, qui, si je n'ai pas réussi à les convertir aux nano-fils, m'ont toujours encouragé dans tout ce que j'ai fait.

Je remercie finalement Rose-Marie, aux côtés de qui la vie est tellement plus belle.

Contents

List of Figures **ix**

List of Tables **xvii**

List of acronyms **xix**

Introduction **1**

Bibliography **5**

1 Porous Anodic Alumina **7**
1.1 History of Porous Anodic Alumina 7
1.2 Fabrication principle and structure tailoring 8
1.2.1 The anodization of aluminium 8
1.2.2 The pore formation mechanism 9
1.2.3 Pore ordering and structure tailoring 10
1.3 Results and discussion 14
1.3.1 The experimental set-up 14
1.3.2 The PAA template fabrication process 16
1.4 Conclusion 28

Bibliography **29**

2 Electrodeposition in PAA **33**
2.1 Introduction and brief state of the art 33
2.2 The principles of electrodeposition 35
2.3 Experiments, results and discussion 36
2.3.1 The experimental setup 36
2.3.2 The pulsed electrodeposition (PED) parameters study 37
2.3.3 Liberating the nanoparticles with PAA etching 45
2.3.4 Water plasma treatment for a better filling with catalysts 46
2.4 Conclusion 54

Bibliography **57**

3 One-dimensional nanostructure growth in PAA **61**
3.1 Definitions and potential applications 61
3.2 One dimensional (1D) nanostructures growth 62
3.2.1 Synthesis methods 62
3.2.2 Growth theory - Influence of the growth parameters 66
3.2.3 Guided growth - Confined growth in porous templates 72
3.3 Experiments, results and discussion 74
3.3.1 The hot wire CVD reactor 74
3.3.2 Influence of some growth parameters 75
3.3.3 CNT growth in PAA 84
3.3.4 TEM investigation and electron diffraction analysis 85
3.3.5 I(V) measurements (proof of concept) 91
3.4 Conclusion 95

Bibliography **97**

4 Fabric. of a porous stack for 1D nanostruct. growth **105**
4.1 Introduction 105
4.1.1 1D nanostructure-based FETs: a state of the art 105
4.1.2 The concept of the vertical FET 107
4.2 The porous stack fabrication 108
4.2.1 Plasma processing in microelectronics 108
4.2.2 Results: the pore etching through Al and SiO_2 114
4.3 1D nanostructure growth inside the porous stack 127
4.3.1 Catalyst electrodeposition in the porous stack 127
4.3.2 CNT growth 134
4.3.3 SiNW growth 136
4.3.4 The electrode printing and the patterned porous stack 140
4.4 Conclusion 157

Bibliography **159**

Conclusion **163**

List of Figures

1.1 Current-time transient during an anodization of a 2" Al sample. 10
1.2 Examples of natural hexagonal arrangement in (a) honeycomb, (b) basaltic columns and (c) dried clay. (d) illustrates the formula below. 11
1.3 (a) Anodization setup for 2" wafers, (b) anodization setup for small samples (1 cm^2) and (c) anodization setup for 2" wafers, with graphite cathode (a), glass coil cooler (b), and glass stirrer (c). 16
1.4 (a) SEM cross-section picture of a PAA template after the second anodization and (b) corresponding FA and SA current-time curves. 18
1.5 SEM cross-sections of PAA anodized at (a) 20 V in sulfuric acid, (b) 40 V in oxalic acid and (c) 140 V in phosphoric acid. The bottom pictures are magnifications from the top ones at the same scale, in order to compare the size of the pores. 19
1.6 Thickness of PAA as a function of the second anodization time. The sample was anodized under 20 V in 0.3 M sulfuric acid. 20
1.7 Cross-section of PAA templates after a second anodization of (a) 2 min, (b) 11 min and (c) 28 min. The three samples are magnified 50 000 times, the inset in (a) is a 100,000x magnification. 20
1.8 Barrier layer thickness (black circles) and pore diameter (red crosses) as a function of the immersion time in H_3PO_4. Anodization took place in oxalic acid at 40 V. 22
1.9 PAA after second anodization (3 min), (a) before the pore widening process, (b) and (c) after a 20 min and 30 min pore widening process, respectively. (d) is the corresponding top-view of (c). 22
1.10 Pore diameter as a function of the pore widening duration, for samples anodized in oxalic acid (black squares) and in sulfuric acid (red circles). . 23
1.11 Evolution of the pore diameter after immersion in 0.3M H_3PO_4 for (a) 5 min, (b) 11 min, (c) 18 min, (d) 23 min 30 sec, (e) 27 min 30 sec, (f) 31 min, (g) 40 min 30 sec and (h) 50 min. 25
1.12 Schematic drawing of the bi-layer structure of the pore walls. The inner wall is oxalate ions-contaminated, and the outer wall is purer alumina. . . 26
1.13 (a) I(t) curve showing the current drop at the end of the anodization and (b) corresponding SEM cross-section. 27

2.1 Drawing of the three-electrode system used for electrodeposition. WE, CE and RE stand for working, counter and reference electrode, respectively. . 36
2.2 Drawing of a pulse used for pulsed electrodeposition experiments. OCP = Open Circuit Potential. 38
2.3 (a) Example of an I(t) curve (only four pulses out of 500 are represented) from a Ni electrodeposition experiment. (b) is a magnified view of one pulse from (a), with the superimposed voltage signal (doted red line). . . . 39
2.4 SEM cross-sections of PAA templates after Cu electrodeposition at -8.5 V. (a) 50 sweeps and (b) 200 sweeps. 40
2.5 (a) SEM top-view of liberated Ni nanowires, after the PAA has been etched away with chromic acid. (b) SEM cross-section of a PAA after a 6000-sweep Ni deposition (the massive overdeposited Ni is clearly visible onto the template). 40
2.6 Current between WE and CE as a function of a sweeping voltage (U_{we}) applied between WE and RE, for a Ni electrodeposition experiment. The silicon substrate resistivity are (a) $\rho < 0.005$ Ω.cm. (b) $\rho =$ 1-10 Ω.cm. . . 41
2.7 SEM cross-sections of PAA after Ni electrodeposition. Top: 1 ms pulses, 500 sweeps and 2500 sweeps, respectively. Bottom: 5 ms, 10 ms and 20 ms pulses, respectively (500 sweeps). 42
2.8 I(t) curves showing the first and the last pulses of (left) 5 ms pulses experiment and (right) 100 ms experiment. 43
2.9 Equivalent charge (obtained integrating I(t) curves) as a function of pulse duration. 44
2.10 SEM cross-section of a PAA after Au electrodeposition. Fifty 5 ms pulses were applied, at -5.5 V. 44
2.11 Evolution of the aspect of Cu NWs after PAA removal with 1 M NaOH. Samples have been immersed for (a) 1 min, (b) 5 min and (c) 20 min. . . 45
2.12 SEM picture of liberated Au particles after PAA removal with 2 M NaOH for 18 min. 46
2.13 Drawing of the plasma chamber with the triode configuration. 47
2.14 Cross-sections of (a) non-treated and (b) and (c) water plasma-treated (for 15 min) PAA after Cu electrodeposition. (c) shows a large zone of 17 µm with a quasi 100% pore filling. 48
2.15 Cross-sections of (a) non-treated and (b) and (c) water plasma-treated (for 40 min) PAA after Cu electrodeposition. 49
2.16 Top views of non-treated samples after Cu electrodeposition and PAA removal with NaOH. The magnification increases from 2000x to 30000x from (a) to (d). 50
2.17 Top views of water plasma-treated (40 min) samples after Cu electrodeposition and PAA removal with NaOH. The magnification increases from 2000x to 30000x from (a) to (d), for an easy comparison with Figure 2.16. 51

2.18 Tilted views of (a) non-treated and (b), (c) water plasma-treated samples after Ni electrodeposition. PAA has been removed with NaOH in (a) and (c). 52
2.19 (a) non-treated and (b) plasma-treated sample after Au electrodeposition. 53
2.20 Pictures of a droplet of water on the surface of (a) a plasma-treated PAA (40 min) and (b) a non-treated PAA. 54

3.1 (a) Au-Si phase diagram. (b) Schematic drawing of a nanowire growing in the VLS mode. 67
3.2 This figure is extracted from [5]. (A) refers to shadow sputtering [91], (B) and (D) to preferential nucleation [89], [90] and (C) to multilayer-based template [92]. 73
3.3 Schematic drawing of the Hot-Wire CVD reactor used for the 1D nanostructure growth. 74
3.4 SEM cross-section of a PAA with Cu catalyst particle, before SiNW growth. 76
3.5 Cu-Si phase diagram, from [111]. 76
3.6 SEM cross-sections of a sample after a growth performed at 540°C, P_f=175 W, 7.5 mbar, H_2:SiH_4 = 100:20 sccm. 78
3.7 SEM top view of a sample after a growth performed at 540°C, P_f=175 W, 4.0 mbar, (a) H_2:SiH_4 = 95:5 sccm, (b) and (c) H_2:SiH_4 = 97.5:2.5 sccm. 78
3.8 SEM cross-sections of a sample after a growth performed at 540°C, 2.5 mbar, P_f=175 W and H_2:SiH_4 = 97.5:2.5 sccm. (a) to (d) some examples of SiNWs with their corresponding Cu particles on their tips, (e) a higher magnification of the enlarged walls due to a-Si deposition. Scale bars in (c), (d) and (e) are 200 nm. 79
3.9 SEM cross-section of a sample after a 1 h growth performed at 490°C, 2.5 mbar, P_f=175 W and H_2:SiH_4 = 97.5:2.5 sccm. 80
3.10 Tilted views of the sample shown in Figure 3.9 after PAA wet etching. The hollow structure is clearly visible in (c). Scale bars are 200 nm. . . . 81
3.11 (a) and (b): SEM cross-section and top-view of the sample before the growth. (c) and (d): same sample after a growth in optimized conditions (see Table 3.1) with the hot wire off. Scale bars are 200 nm. 82
3.12 (a) and (b) SiNW growth evidence in SEM cross-sections and (c) tilted view of the Si vertical rods supporting a-Si crust. Scale bars are 200 nm. . 82
3.13 SEM cross-section of a PAA after a growth under 1 mbar (540°C, H_2:SiH_4 = 97.5:2.5 sccm, and P_f=175 W. 83
3.14 Top-views of a PAA after a 30 minute growth, performed at 500°C, H_2:CH_4 = 50:50 sccm, p = 50 mbar and P_f=180 W. Some CNTs protruding out of the PAA are visible in the bottom-right image (yellow arrows). 84
3.15 Comparative schematic drawing of TEM and SEM principle [112]. 85

3.16 (a) and (b) TEM picture of a SiNW grown at 540°C. (b) Drawing of (a), angles between the two kinds of twins, and between the twins and the wire surface are reported. (c) Electron diffraction pattern of the wire shown in (a). The angles and distances measured to identify the crystallographic planes are shown. 87
3.17 Left: high magnification TEM picture of the Figure 3.16(a) and right: corresponding oriented EDP with the construction lines used to determine the growth direction of the nanowire. 88
3.19 Three TEM pictures of SiNWs with highlighted twin orientations. 89
3.18 Left: a SiNW grown at 540°C and right: corresponding EDP revealing the diffraction planes. 89
3.20 (a) TEM picture of a SiNW exhibiting a catalyst particle at its tip (dark hemisphere) and (b) HR-TEM picture of a SiNW grown at 490°C. 90
3.21 Electron diffraction pattern of amorphous SiNWs. 90
3.22 TEM picture of a SiNW exhibiting two distinct parts, with their corresponding EDPs. 91
3.23 Amorphous SiNTs, formed from the a-Si deposition on the pore walls during the growth, with their corresponding EDP in the inset. 91
3.24 (a) Drawing of the principle of the electrical measurement and (b) I(V) curve for a measurement performed before the SiNW growth with two probes connected to the top of the PAA, and to the Si substrate, respectively, according to (a). 92
3.25 I(V) curve of a Si substrate, both probes connected to it. Our Keithley system saturates for currents superior to 10 mA. 93
3.26 (a) SEM cross-section and (b) top view of a PAA template after a SiNW growth at 450°C, 5 mbar and with H_2:SiH_4 = 90:10 sccm. (c) and (d) Tilted views of the same sample after PAA removal. (e) I(V) curve for a measurement performed after the SiNW growth with two probes connected to the top of the PAA, and the Si substrate, respectively. Scale bars in (a), (c) and (d) are 400 nm. 94
3.27 SEM top views of a PAA sample after a SiNW growth (a) before and (b) after the a-Si crust etching. 94

4.1 (a) Planar configuration and (b) vertical configuration of NW-based FETs, as described in [24] and [20], respectively. 106
4.2 3D diagram of the porous stack. The 1D nanostructures (light-blue) grow in the vertical pores that provide the gate contact (Al, dark blue) and insulating layers between the source and drain electrodes. 107
4.3 Schematic diagram of the formation of a plasma sheath close to the electrodes. Electrons accumulate in the electrode because of DC field isolation, and thus attract positive ions. 110
4.4 (a) Classic parallel plates RIE reactor and (b) ICP RIE reactor. 111

4.5 SEM cross-section of a Si substrate etched with a PAA layer as a mask, from [32]. Scale bar is 200 nm. 112
4.6 Schematic diagram of the Bosch process. The bottom of the trench, which can be as small as 20 nm large in our case, is etched while the side walls are protected by the passivation layer. The passivation layer thickness is not to scale. 113
4.7 SEM cross-sections of PAA on an Al layer after an Al etching with different Ar:Cl_2 ratios. From [37]. 115
4.8 Al (black squares) and PAA (red triangles) thickness as a function of etching duration. 116
4.9 SEM cross-sections of PAA after (a) 6 min, (b) 10 min, (c) 13 min and (d) 15 min ICP etching of the Al layer. 116
4.10 SEM cross-section of a PAA template after a 4'30 etching. White arrows indicate the places where Al has been etched, corresponding to places where barrier layer has been removed. The inset is a magnification of the central part of the picture. 117
4.11 (a) Thin PAA ($\approx$ 85 nm thick) on an Al layer before the Al etching and (b) porous Al layer after a 2 min etching. The PAA has disappeared, leaving the porous Al ($\approx$ 170 nm thick) unprotected. 118
4.12 SEM cross-sections of a stack after an SiO_2 etching. Only a few pores go through the SiO_2 layer entirely. From [37]. 119
4.13 SEM cross-sections of 500 nm-thick SiO_2 layer with a PAA mask (a) before the SiO_2 etching, (b) and (c) after the 30 s SiO_2 etching. The white arrows in (a) indicate some places with remaining barrier layer, and the white dotted line in (c) marks the Al/SiO_2 interface. 120
4.14 SEM cross-sections of 500 nm-thick SiO_2 layer etched through a PAA mask for (a) 1 min, (b) 2 min and (c) 3 min. 120
4.15 SiO_2 pore height (black squares) and PAA thickness (red triangles) as a function of etching duration. 121
4.16 SEM top-view of the surface of a SiO_2 layer after a 3 min etching through a PAA mask and its subsequent removal. (a) is magnified 20 000 times and (b) is magnified 90 000 times. 122
4.17 SEM cross-sections of an SiO_2 layer (a) before and (b), (c) after an RIE etching. (b): 8 min and (c): 16 min etching with CF_4:C_4F_8:O_2 = 45:15:10 sccm. 122
4.18 SEM cross-section of an SiO_2 layer under a PAA after an 8-min SiO_2 etching with CF_4:SF_6:O_2 = 45:5:10 sccm. 123
4.19 SEM cross-sections of an SiO_2 after a short barrier layer etching performed by ICP RIE, followed by a simple SiO_2 RIE. 123
4.20 SEM cross-sections of a stack after a 3 minutes Al ICP etching. The white arrows and circle show some of the many little holes in the SiO_2 layer. . . 125

4.21 (a) SEM cross-section of a porous stack after the 2 min SiO_2 etching and (b) same sample as after PAA and Al dissolution (some Al parts remain on the SiO_2 surface). 125
4.22 SEM cross-sections of a stack after (a) 2 min, (b) 3 min and (c) 4 min SiO_2 etching. 126
4.23 SEM cross-section of a stack realized on a 2 inches wafer. PAA, Al and SiO_2 layers are 160, 180 and 100 nm-thick, respectively. 127
4.24 SEM cross-sections of a porous stack after Ni electrodeposition under optimized conditions. 128
4.25 Illustration of the importance of the silver paste contact during the electrodeposition. On the left, a proper contact leads to a deposition at the bottom of the pores (though very limited here), whereas a contact on the edges (on the right) reduces cations in the Al pores. 129
4.26 SEM cross-sections of a porous stack after Au electrodeposition under optimized conditions of chapter 2. (a) 1000 sweeps, (b) 50 sweeps and (c) 20 sweeps. 130
4.27 (a) SEM cross-section and (b) top view of a porous stack after Au electrodeposition under optimized conditions of chapter 2. Au is properly deposited, with no deposition on the surface of the sample. 130
4.28 (a) SEM cross-section and (b) top view of a porous stack after Cu electrodeposition: 1000 sweeps of 5 ms, at -8.5 V. The white arrows in (a) indicates the few Cu particles visible at the bottom of the pores. 131
4.29 Partial I(t) curves from a typical Au electrodeposition on (red curve) 1-10 Ω.cm substrate with the back SiO_2, (blue curve) 1-10 Ω.cm substrate without the back SiO_2 and (green curve) $<$ 0.005 Ω.cm substrate without the back SiO_2. 132
4.30 SEM cross-sections of a porous stack after a typical Au electrodeposition (50 sweeps at -5.5V) on a (a) 1-10 Ω.cm substrate with the back SiO_2, (b) 1-10 Ω.cm substrate without the back SiO_2 and (c) $<$ 0.005 Ω.cm substrate without the back SiO_2. 132
4.31 Four I(t) curve extracts, from Au electrodeposition at -3.5 V, -2.5 V, -1.5 V and -0.5 V. 50 sweeps have been applied in each case. Corresponding SEM pictures are visible under each I(t) curve. 133
4.32 Cross-section of a sample after a Ni electrodeposition (-1.5 V, 100 sweeps) on low resistivity substrate. 134
4.33 (a) SEM pictures of a porous stack after a 15-minute CNT growth performed in the conditions described in Table 4.4. (b) Same sample as in (a) but without catalyst particle: no CNT is visible after the growth. . . . 135
4.34 SEM top views (top) and cross-sections (bottom) or porous stacks after a (a) 3'30, (b) 2'20 and (c) 1'00 CNT growth. 136
4.35 SEM pictures showing protruding CNTs after CNT growths. (a) and (b) have been taken after the 3'30 growth, and (c) after the 2'20 growth. . . . 136

4.36 SEM pictures of the porous stack after a SiNW growth at 470°C for SiH_4:H_2 = (a) 5:95, (b) 10:100, (c) 15:85 and (d) 20:100 sccm. The bottom pictures in (a) and (c) correspond to reference samples (Au nano-particles on Si substrate) . . . 138
4.37 SEM pictures of the porous stack after a SiNW growth at 450°C for SiH_4:H_2 = 20:100 sccm. . . . 139
4.38 SEM pictures of the porous stack after a SiNW growth at 500°C for SiH_4:H_2 = 10:100 sccm. . . . 139
4.39 SEM cross-sections of a porous stack after the electrode printing at (a) 12 V and (b) 18 V. . . . 141
4.40 SEM cross-sections of a porous stack after the electrode printing on heated substrates. Small particles are visible inside the pores. . . . 142
4.41 SEM pictures of the o-ring area (inside and beyond) after the anodization step and the Al RIE. . . . 143
4.42 Experimental setup for selective anodization, as used in [39]. . . . 144
4.43 Global process of the localized formation of the porous stack using photoresist as a mask. Thicknesses are not to scale. . . . 145
4.44 Some examples of patterns we designed for the SiO_2 mask etching. (a) Design software views and (b) optical microscope pictures of the alignment crosses after the resist development. Scale bars in (a) are 200 nm. . . . 146
4.45 SEM top-views of (a) a PAA after a one-step anodization (cross-section in the inset), (b) a PAA after a one-step anodization and a 9-min pore widening (c) the Al surface formerly covered with photoresist. . . . 146
4.46 (a) Cross-section and (b) top-view of the transition zone between the PAA and the protected Al. (c) Magnifications of specific parts of the transition zone. . . . 147
4.47 First anodization (FA) and second anodization (SA) I(t) curves corresponding to the PAA formation with photoresist as a barrier (the whole SA lasted about 8 min). . . . 148
4.48 SEM top views of a sample after a two-step anodization of (a) the surface under the resist and (b) in the unprotected patterns. . . . 148
4.49 (a) FA and SA I(t) curves corresponding to the PAA formation with photoresist as a barrier, with a shorter SA. (b) Al surface after two-step anodization and resist removal. . . . 149
4.50 SEM cross-sections of a PAA in the transition area after a two-step anodization. (a) is in the unprotected area and (b), (c), and (d) correspond to what one can see as we head for the protected area. Note that third picture is magnified for the sake of visibility and that the scale is therefore different. . . . 149
4.51 PAA formed under the resist, that has been deposited between the first and the second anodization to avoid PAA removal. The PAAs are very thin, especially in (b), where one can see it follow the curve of the underlying Al layer. . . . 150

4.52 Single long anodization I(t) curve corresponding to the PAA formation with photoresist as a barrier. 151
4.53 SEM cross-sections taken at different places of a sample after a one-step anodization and a 6 min Al etching. (a), (b) and (c) show some large thickness disparities in the PAA and the Al layer. 151
4.54 Global process of the localized formation of the porous stack using SiO_2 as a mask. Thicknesses are not to scale. 153
4.55 SEM pictures of some patterns realized in a SiO_2 layer. The SiO_2 etching recipe is the first one in Table 4.7, and similar results have been obtained with the second and third recipes. Badly defined etchings are particularly visible in (c), in the corners of the crosses. 154
4.56 SEM pictures of some patterns realized in a SiO_2 layer, etched with the fourth recipe of Table 4.7. (c) and (d) show the edge of the SiO_2 mask in cross-section and top view, respectively. 155
4.57 (a) First and second anodization I(t) curves of a sample anodized through a 500-nm thick SiO_2 mask. (b) SEM top view of the as-formed PAA after the SA. 156
4.58 SEM cross-sections of a PAA realized through a 500-nm thick SiO_2 mask: (a) in the middle of a pattern, (b) and (c) near the boundary with the SiO_2 mask. 156
4.59 SEM cross-sections of a stack after (a) the two-step anodization and the Al etching, (b) the SiO_2 etching. (a) and (b) are in the middle of a pattern and (c) shows the boundary with the SiO_2 mask after Al and SiO_2 etchings. The white arrow points out the very last visible pores. 156

List of Tables

1.1 Summary table of the anodization and etching conditions. 28

2.1 Standard reduction potential are given with respect to the SHE. 37

3.1 Optimized growth conditions for SiNW growth in PAA in our HW-CVD reactor. 80

4.1 Optimized conditions for Al etching through a PAA mask in our ICP reactor. 115
4.2 Optimized conditions for SiO_2 etching through a PAA mask in our ICP reactor. 119
4.3 Summary table of the SiO_2 etchings performed in a simple RIE reactor. . 124
4.4 CVD growth conditions for CNT growth in the porous stack in our HW-CVD reactor. 135
4.5 Summary table of the SiNW growths carried on in the porous stack. . . . 137
4.6 Summary table of the printing conditions we used to realize electrodes on a porous stack. 140
4.7 Summary table of the four recipes we tried to realize openings in the SiO_2 mask. 153
4.8 Comparative table of the two methods we tried to realize localized porous stack. 157

List of acronyms

a-Si	Amorphous silicon
CE	Counter Electrode
CMOS	Complementary Metal-Oxide-Semiconductor
CNT	Carbon Nanotube
CVD	Chemical Vapor Deposition
EBL	Electron Beam Lithography
ECR	Electron Cyclotron Resonance
EDP	Electron Diffraction Pattern
FA	First Anodization
FET	Field Effect Transistor
GAA	Gate All Around
HA	Hard Anodization
HW(CVD)	Hot Wire (Chemical Vapor Deposition)
ICP	Inductively Coupled Plasma
ITO	Indium-Tin Oxide
LSV	Linear Sweep Voltage
MA	Mild Anodization
MBE	Molecular Beam Epitaxy
MWNT	Multi-Wall Nanotube
NT	Nanotube
NW	Nanowire
OCP	Open Circuit Potential
PAA	Porous Anodic Alumina
PECVD	Plasma-Enhanced Chemical Vapor Deposition
PED	Pulsed Electrodeposition
RE	Reference Electrode
RIE	Reactive Ion Etching
SA	Second Anodization
SEM	Scanning Electron Microscope
SHE	Standard Hydrogen Electrode
SiNW	Silicon Nanowire
SWNT	Single Wall Nanotube
TEM	Transmission Electron Microscope
VSS	Vapor-Solid-Solid
VLS	Vapor-Liquid-Solid
WE	Working Electrode

Introduction

Since the first part of the XXth century and the possibility to observe, fabricate, and work with objects smaller than a few hundreds of nanometers, many scientists have bustled about understanding nano-objects, especially their behaviour and their numerous properties. As the observation techniques were getting improved, a lot of new interesting properties have been revealed among the freshly-discovered nanoparticles until today. One of the most emblematic ones concerns the famous discovery of the carbon nanotubes in 1991, which electrical, mechanical or optical properties goes far beyond any material known so far. Some other studies showed for example that specific nanoparticles could have huge benefits in medicine (improved drug delivery accuracy, medical imaging...), health (antimicrobial nano-silver), environment (water filtration), energy (higher Li-ion batteries density storage, solar cells...), electronics (components size decrease, lower power consumption), mechanics (stronger materials, better elasticity...) and in many other domains.

The wide variety of the different nanoparticles can be subject to a classification, based on their morphological appearance. We find nanowires, nanotubes, nanoribbons, nanosheets, nanospheres... The nanowires and the nanotubes can be merged under the appellation "one dimensional nanostructures", or 1D nanostructures. They are called this way from their high aspect ratio, their diameter varying between 1 nm to a few tens of nm, and their length up to hundred microns. So far, 1D nanostructures have been studied by a lot a research teams in the world, for their potential and promising applications, notably in electronics. Indeed, it has been shown that they could be used as basic building blocks in nanoscale electronic devices, such as transistors, sensors, photodetectors, solar cells, field emitters..., which can avoid the use of costly patterning techniques. To make good use of the bottom-up formation of these structures allows the fabrication of ready-to-use nanometric elements, whose geometrical features and physical properties can be adjusted, and their implementation in electronic devices made easier.

Despite these promising marches, an essential problem remains to be studied. One cannot handle nanoparticles as easily as tweezers move a grain of sand, so a challenging task consists in being able to control the location and the orientation of the 1D nanostructures, whose interactions with matter are quite different compared to what happens in the macroscopic world. Expensive and time-consuming means like e-beam lithography have been used to define precise spots to grow nanowires, or even to etch nanowires from a bulk material, but this is suitable for demonstrators only, and probably not for mas-

sive integration nor collective organization. Self-organized templates (see intro of [1] for examples) are promising candidates to provide the advantages required for controlled 1D nanostructure growth. In particular Porous Anodic Alumina (PAA) templates, which gather easy and cheap fabrication, geometry flexibility and which can provide collective control of the nanostructures. A PAA template consists in a nanoporous structure, whose vertical and parallel pores can be arranged in a hexagonal pattern, very close to a honeycomb structure. Its fabrication, made by anodic oxidation of aluminium, is simple, cheap, and leads to a periodic hollow formation able to guide the growth of vertical nanostructures, which are confined inside the pores. The nanostructures thus adopt the pore diameter and the spacing corresponding to the inter-pore distance, which are both parameters easily tunable during the PAA fabrication. This powerful tool also makes collective contact easier. Note that the use of PAA templates is in accordance with an integration in the electronic device fabrication industry, since Al is a really common material in this sector.

That's the way many researchers focused on growing nanotubes (NTs) and/or nanowires (NWs) inside PAA templates, leading the path towards ultra-high density integration of individual nanostructures per cm. These studies allowed both metallic and semiconducting materials growth like Si, Ge, C, GaN, InSb, Cu, Ni, Au, Te and many others. It has also been reported that as well as the composition, the morphological aspect of the 1D nanostructures could be modified. Nanotubes or nanowires can be synthesized, in a single stem or with a branched structure thanks to an appropriate design of the template, which is interesting for interconnection applications [2]. An application directly related to the porous template-assisted nanostructure growth has been reported in 2001, when vertically-aligned and patterned carbon nanotubes (CNTs) have been used as field emitters [3], [4]. The same year, CNT-based nanotransistors have been fabricated using a PAA template to grow and contact properly each end of the CNTs [5], which led to a potential density of 2.10^{11} per cm^2. Combining the sensing properties of CNTs and the high order of the vertical pores in PAA, another research team developed a simple process to fabricate parallel sensing channels, responsive to NH_3 and NO_2 [6]. Another interesting field to investigate is the magnetic properties of 1D nanostructures. The latter are indeed a promising candidate for high density magnetic data storage devices, and this is why studies involving classical magnetic materials like Fe, Ni or Co are carried out, using electrodeposition methods to grow metallic nanowires in PAA templates [7], [8], [9]. PAA templates have therefore huge potentialities in the nanomaterials fabrication techniques, and appear like a tool that cannot be ignored for organizing 1D nanostructures, in preparation for high density electronic device integration.

Following the examples cited above, we investigated the CNT and the silicon NW (SiNW) growths inside vertical PAA templates, except we kept in mind a particular goal: to realize a vertical CNT/SiNW-based Field Effect Transistor (FET).

Some very interesting results have already been published and bring a proof of concept about the use of 1D nanostructures in FETs. The most represented structures are definitely SiNWs, that have been successfully used to fabricate transistors. As an emblematic example, Lieber's group used laser ablation (see chapter 3) to synthesize high

quality SiNWs and contacted them by e-beam lithography to make various electronic devices[10], [11]... CNT-based FETs have also been reported but researchers come up against the inability to perform a selected growth of semiconducting CNTs. One can nevertheless cite essential articles like [12] and [13].

A common major drawback of these device fabrication processes is that they mostly consist in in-plane devices, that either require a painful step of transfer and/or alignment [14], implying random connections with pre-patterned electrodes, or impose an electrode deposition according to an anarchic placement of the nanostructures [15], which is unacceptable for more complex integrated circuits. Moreover, even though lithography may be avoided thanks to the bottom-up synthesis, it is still used to contact the NWs (e-beam lithography), and the location of the devices is poorly controlled.

All these devices also suffer from a non-ideal gate coupling (due to their position regarding the bottom or the top gate). To provide a better gate coupling, some innovative configurations have been proposed, like multiple-gate FETs [16], surrounding gates [17]... Besides, some of them have the advantage to integrate more devices thanks to the vertical configuration [18]. The achievement that resembles the most to our goal has been described in [19], where SiNWs are grown vertically and are surrounded by a gate, but there is still a high dependence on the size dispersion of the catalyst droplets, which leads to a badly-controlled SiNW diameter.

The work we present herein takes particular care in describing how to combine the advantages of 1D nanostructures and those of PAA. We propose a configuration that no longer requires heavy and costly means to achieve both placement control and size control. Indeed, the use of a PAA template to guide the nanostructure growth ensures a very narrow diameter distribution, a perfect alignment and a very good spatial spread of the NWs. Moreover, since their position is given by the template during the growth, no subsequent step of dispersion, drop-casting or spraying is required. Basing on the self-arrangement of the PAA, a fully-surrounding gate has been etched, thus providing a quasi-ideal coupling with the nanostructures. The power of this configuration is that the nanostructures directly grow on an electrode, and are immediately organized thanks to the template. The vertically-packed configuration can lead to high densities, up to 10^{11} devices per cm^3, and the confinement of the growing structures allows a modulated doping profile along the axis, which can form p-n junctions in a single NW.

Basically, the outline of this work corresponds to the main steps of the total process to reach this goal; therefore we chose to explain our studies about PAA templates in the first chapter. Their formation process and the experimental methods we used will be detailed, as well as how to customize their geometry. The second chapter will describe the electrodeposition process, that we used to deposit metallic particles at the bottom of the pores of the PAA templates. If, as mentioned above, possible applications can be found in the magnetic data storage field, we performed this study with a view to using metallic nanoparticles as catalysts for CNT and SiNW growth. We therefore investigated Ni, Cu, and Au electrodeposition. In the third chapter we will talk about 1D nanostructure growth, we will introduce our experimental CVD set-up, and show our results about the peculiar case of growth inside PAA templates. For a better understanding, a theoretical

section about catalytic nanostructure growth introduces this chapter. Finally, the fourth chapter will deal with the concept of porous stack. Indeed, to realize a vertical FET, a new structure has been imagined and patented a few years before this work, in order to receive the nanostructures and play the role of electrodes all in the same time. A first part is dedicated to the fabrication principle of the porous stack, that relies on the use of a PAA template as a hard mask for etching vertical pores inside two underlying layers. Then a second part details our results about growth inside the porous stack, last brick in the vertical FET fabrication process. With a view to performing electrical measurements on these samples, a simple lithography-based method has also been developed to narrow the surface where the porous stack is fabricated, and thus create some clean Al contacts. A final part sums up the chapters, and brings some perspectives to this work.

Bibliography

[1] S. Mátéfi-Tempfli, M. Mátéfi-Tempfli, A. Vlad, V. Antohe, and L. Piraux, "Nanowires and nanostructures fabrication using template methods: a step forward to real devices combining electrochemical synthesis with lithographic techniques," *Journal of Materials Science: Materials in Electronics*, vol. 20, pp. 249–254, Jan. 2009.

[2] G. Meng, F. Han, X. Zhao, B. Chen, D. Yang, J. Liu, Q. Xu, M. Kong, X. Zhu, Y. Jung, Y. Yang, Z. Chu, M. Ye, S. Kar, R. Vajtai, and P. Ajayan, "A general synthetic approach to interconnected Nanowire/Nanotube and Nanotube/Nanowire/Nanotube heterojunctions with branched topology," *Angewandte Chemie International Edition*, vol. 48, pp. 7166–7170, Sept. 2009.

[3] S.-H. Jeong, H.-Y. Hwang, K.-H. Lee, and Y. Jeong, "Template-based carbon nanotubes and their application to a field emitter," *Applied Physics Letters*, vol. 78, no. 14, p. 2052, 2001.

[4] S.-H. Jeong and K.-H. Lee, "Fabrication of the aligned and patterned carbon nanotube field emitters using the anodic aluminum oxide nano-template on a si wafer," *Synthetic Metals*, vol. 139, pp. 385–390, Sept. 2003.

[5] W. B. Choi, J. U. Chu, K. S. Jeong, E. J. Bae, J.-W. Lee, J.-J. Kim, and J.-O. Lee, "Ultrahigh-density nanotransistors by using selectively grown vertical carbon nanotubes," *Applied Physics Letters*, vol. 79, pp. 3696–3698, Nov. 2001.

[6] H. Y. Jung, S. M. Jung, J. Kim, and J. S. Suh, "Chemical sensors for sensing gas adsorbed on the inner surface of carbon nanotube channels," *Applied Physics Letters*, vol. 90, pp. 153114–153114–3, Apr. 2007.

[7] A. J. Yin, J. Li, W. Jian, A. J. Bennett, and J. M. Xu, "Fabrication of highly ordered metallic nanowire arrays by electrodeposition," *Applied Physics Letters*, vol. 79, pp. 1039–1041, Aug. 2001.

[8] H. Zeng, M. Zheng, R. Skomski, D. Sellmyer, Y. Liu, L. Menon, and S. Bandyopadhyay, "Magnetic properties of self-assembled co nanowires of varying length and diameter," *David Sellmyer Publications*, May 2000.

[9] Q. Xu, G. Meng, X. Wu, Q. Wei, M. Kong, X. Zhu, and Z. Chu, "A generic approach to desired metallic nanowires inside native porous alumina template via redox reaction," *Chem. Mater.*, vol. 21, no. 12, pp. 2397–2402, 2009.

[10] Y. Cui and C. M. Lieber, "Functional nanoscale electronic devices assembled using silicon nanowire building blocks," *Science*, vol. 291, pp. 851–853, Feb. 2001.

[11] Y. Huang, "Logic gates and computation from assembled nanowire building blocks," *Science*, vol. 294, pp. 1313–1317, Nov. 2001.

[12] S. J. Tans, A. R. M. Verschueren, and C. Dekker, "Room-temperature transistor based on a single carbon nanotube," *Nature*, vol. 393, pp. 49–52, May 1998.

[13] R. Martel, T. Schmidt, H. R. Shea, T. Hertel, and P. Avouris, "Single- and multi-wall carbon nanotube field-effect transistors," *Applied Physics Letters*, vol. 73, pp. 2447–2449, Oct. 1998.

[14] Y. Huang, "Directed assembly of one-dimensional nanostructures into functional networks," *Science*, vol. 291, pp. 630–633, Jan. 2001.

[15] Z. Zhong, D. Wang, Y. Cui, M. W. Bockrath, and C. M. Lieber, "Nanowire crossbar arrays as address decoders for integrated nanosystems," *Science*, vol. 302, pp. 1377–1379, Nov. 2003.

[16] J.-T. Park and J.-P. Colinge, "Multiple-gate SOI MOSFETs: device design guidelines," *Electron Devices, IEEE Transactions on*, vol. 49, no. 12, pp. 2222–2229, 2002.

[17] H. T. Ng, J. Han, T. Yamada, P. Nguyen, Y. P. Chen, and M. Meyyappan, "Single crystal nanowire vertical surround-gate field-effect transistor," *Nano Lett.*, vol. 4, no. 7, pp. 1247–1252, 2004.

[18] J. Goldberger, A. I. Hochbaum, R. Fan, and P. Yang, "Silicon vertically integrated nanowire field effect transistors," *Nano Lett.*, vol. 6, pp. 973–977, Oct. 2006.

[19] V. Schmidt, H. Riel, S. Senz, S. Karg, W. Riess, and U. Gösele, "Realization of a silicon nanowire vertical surround-gate field-effect transistor," *Small*, vol. 2, no. 1, p. 85–88, 2006.

Chapter 1

Porous Anodic Alumina

1.1 History of Porous Anodic Alumina

An anodization process corresponds to an electrochemically-assisted oxidation of a metal. Aluminium oxidation has been well-known for several decades now, forasmuch as since the beginning of the XXth century, the protective power of aluminium oxide upon objects made of aluminium against corrosion has been demonstrated. Anodization is also efficient to colorize aluminium, which has made this technique widely used in industry for decades now. More recently, i.e from the 50s, anodic aluminium oxide aroused new interest with the emergence of electron microscopy, which led to the study of the alumina pores formation. A lot of articles have been published since then, from formation theory to practical fabrication. The first model describing the pore structure, introducing the concept of hexagon cells, has been brought by Keller et al. in 1953 [1]. Then research teams like Thompson, Wood et al. [2],[3] brought precise explanations about the chemical mechanisms involved in the pore formation process, especially about ionic exchanges at the alumina/aluminium and the alumina/electrolyte interfaces. Tremendous understandings of the different structures obtainable depending on voltages, electrolytes, temperature etc. have thus been done between 1970 and the 90s. A break-through in ordering alumina pores has been made in 1995 by Masuda and Fukuda, who managed to fabricate mono-domain porous alumina areas over large surfaces [4]. First using a "two-step replication", and then using a nano-imprint technique [5], porous alumina templates exhibiting high aspect ratio with both adjustable diameters and narrow diameter distribution were easy to realize. Other metals like Ti [6], W [7], Ta [8], Zr [9]... have also been oxidized to form porous structures, nevertheless none of them has led to as many studies as Porous Anodic Alumina (PAA). However, although advances in the field of nano-ordering have leaped forward during these decades, the use of PAA is nowadays still restricted to research labs, where numerous potential applications are still being developed. The goal of the following is to explain the formation theory of a PAA template, and then to use it to carry out and understand our investigation about it. We especially took particular care to fabricate ordered templates with various pore diameters, height, and to control the thickness of the barrier layer present at the bottom of the pores.

1.2 Fabrication principle and structure tailoring

1.2.1 The anodization of aluminium

Contrary to natural aluminium oxidation, which is due to the presence of oxygen in the atmosphere, the anodization is an electrochemical process, and therefore involves an electric field that influences the reaction a lot. Indeed, without any electric field, the thin aluminium oxide (alumina) layer that forms according to:

$$4\,Al_{(s)} + 3\,O_{2(g)} \longrightarrow 2\,Al_2O_{3(s)}$$

stops the reaction as soon as the alumina is thick enough (a few nanometers) to prevent oxygen of the atmosphere to react with aluminium. In the electrochemistry case, the electric field helps ions to cross the oxide barrier, allowing the reaction to go further and therefore to realize thicker alumina layers, as long as the electric field is high enough compared to the barrier thickness. This process has been used for ages to realize protective films on metals (especially aluminium) against corrosion. From a practical point of view, the aluminium to oxidize is set as the anode, and a counter electrode (typically made of graphite, platinum or gold so it doesn't react in the electrolyte) as the cathode. Both are dipped in the electrolyte, usually made of acid (sulfuric, oxalic, phosphoric...) diluted in DI water. The oxidation of Al is as follows:

$$Al_{(s)} \longrightarrow Al^{3+} + 3\,e^-$$

This reaction takes place at the metal/oxide interface and is responsible of the alumina formation. Indeed, part of the Al^{3+} ions supplied by this reaction crosses the oxide barrier thanks to the electric field, and then dissolve in the electrolyte, but the other part will react with oxygen-containing ions (O^{2-} and OH^-) and will form alumina. The origin of these oxygen-containing ions is still discussed, at least their proportion, for they could come from at least two distinct reactions:

$$H_2O \longrightarrow H^+ + OH^- \text{ and}$$
$$H_2O \longrightarrow 2\,H^+ + O^{2-} \text{ [10]}$$

In both cases the anions would mainly come from water dissociation at the electrolyte/oxide interface. The anodization process can be written as follows:

$$2\,Al_{(s)} + 3\,H_2O_{(l)} \longrightarrow Al_2O_{3(s)} + 3\,H_{2(g)} \text{ [11]}$$

though this equation is a simplified view of what really happens during the whole process. If the electrolyte used in this reaction is neutral or basic (i.e pH > 5 [10], [11]), the alumina layer is called barrier-type alumina, which is a classical thin layer (up to several microns) on the non-oxidized aluminium. On the contrary, if an acidic solution (typically sulfuric, oxalic or phosphoric acid) is used as an electrolyte, the as-formed alumina is also partially dissolved, due to a proton-assisted mechanism [12]. Under very specific conditions, this can lead to the formation of porous-type alumina: this is the object of the next paragraph.

1.2.2 The pore formation mechanism

In this section we only focus on aluminium anodization performed inside an acidic electrolyte. As mentioned before, we attend two electric field-assisted reactions:

- the alumina formation (see above) at the metal/oxide interface,
- the alumina dissolution at the electrolyte/oxide interface: alumina is dissolved by the acidic electrolyte, assisted by the electric field that extracts Al^{3+} ions from the alumina, which supplies oxygen-containing anions on top of the other source mentioned above.

Of course if one of the two reactions above prevails, the pore formation cannot take place. In one case we would have the formation of barrier-type alumina, which has already been dealt with, and in the other case no alumina would be formed at all, thus giving way to a pure aluminium surface. The porous alumina can only form if these two reactions balance. Both reactions are electric field-enhanced, and therefore the voltage applied during the anodization process will play a crucial role in this equilibrium.

Before describing the mechanisms occurring during the formation of anodic alumina, a few words have to be told about the mechanical stress linked to the oxidation of an aluminium layer. Usually, the insertion of atoms, impurities or dopants in a material leads to a volume expansion of the latter. In the case of aluminium, the insertion of oxygen atoms is generally followed by a volume expansion of a factor between 1 and 2, depending on the conditions [13]. This volume expansion results in a mechanical stress inside the alumina, which is believed to be the cause of the irregularities on the surface of the oxide. Thus, even after a barrier-type oxidation, due to stress relaxation in alumina, the surface reveals a roughness.

To understand better what happens during the pore formation process, one has to decompose the mechanism. It is also very helpful to follow the evolution of the current as anodization goes along (see Figure 1.1).

At the very beginning, a flat aluminium layer deposited on a substrate is immersed in an acidic electrolyte. Natively a thin (2-3 nm) oxide layer is already present. Once a voltage is applied between this sample and the cathode, the anodization of aluminium immediately begins, both at the metal/oxide and at the oxide/electrolyte interfaces [12]. This is due to the electric field, which accelerates the oxidative species (O^{2-} and OH^{-}) through the barrier layer, and Al^{3+} ions that are extracted from the barrier oxide. The oxide layer thus gets thicker, which results in a dramatic current decrease (stage I in Figure 1.1). As we have seen above, the aluminium oxide formation is always accompanied by a volume expansion, which involves a lot of stress and irregularities in the material. This results in the creation of a roughness at the oxide/electrolyte interface, quite bigger than the roughness of the initial aluminium layer and sufficient to reveal differences of alumina thickness. As a result, the resistance of the alumina is not homogeneous anymore, and the field lines will naturally point at the thinner areas, where ions exchanges will therefore be easier. In these places, the high electric field ($\approx 10^7$ V.cm^{-1} [14]) weakens Al-O bonds and extracts Al^{3+} ions from alumina more easily than in thick oxide

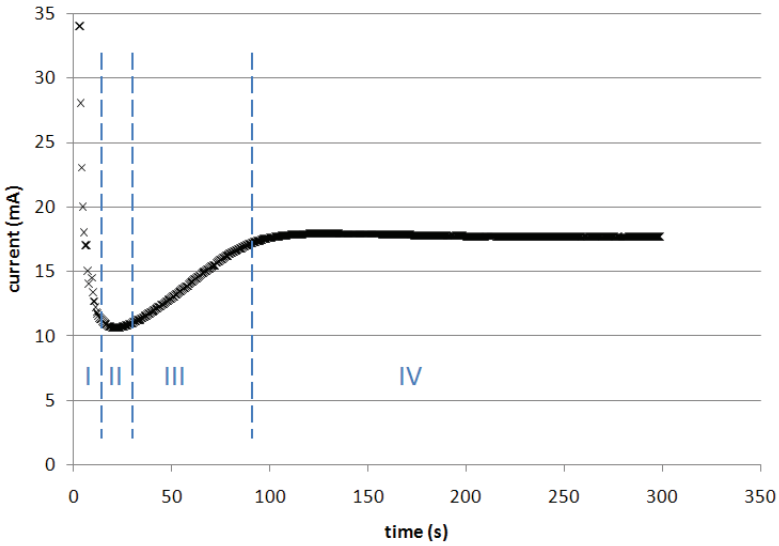

Figure 1.1: Current-time transient during an anodization of a 2" Al sample.

areas, which leads to a faster dissolution of alumina. Thus individual paths will form [15], which will make the current increase (stage III in Figure 1.1), after having reached a minimum (stage II) corresponding to the maximum thickness of the oxide layer. These paths announce the places of the future pores, that will grow during the steady-state (stage IV), when the equilibrium between the dissolution of alumina and its formation is reached. Note that the thin oxide areas are the only places where both alumina dissolution and formation balance, which leads to the digging of pores through the sample. The coexistence of these two phenomena can be decomposed as follows: the field-enhanced dissolution of alumina makes the anodization current become high enough to create a new oxide layer. Little by little, the thickening of the oxide slows down the ion transfer, which allows the alumina dissolution to become the predominant reaction again. As long as the conditions are maintained, this cycle will continue until the aluminium layer is completely consumed. Of course, it is possible to stop the process in order to keep an aluminium layer underneath the porous alumina, whose height depends on the anodization duration. On stage IV, one can notice that the current slightly decreases. The anodization current being mainly related to ionic movement through the barrier oxide [15], diffusion limits in this area are reflected on the current evolution during the steady state. Depending on the cases, the steady-state current can be more or less constant, and can even slightly increase.

1.2.3 Pore ordering and structure tailoring

For many applications, other porous templates than porous alumina exist and are commercially available, such as polymer-based porous templates (usually fabricated by the

track-etched process). Besides their obvious advantages that are ease of use, constancy, and reliability, we nevertheless put the emphasis on the complete customized fabrication (thickness, pore diameter...) of our membranes, which is not possible with commercial products. Moreover, the lower thickness of these porous membranes are usually larger than the thickness we will actually use in this work, which make the PAA a candidate of choice.

In the following, we will see how we can play with the different experiment parameters to fabricate PAA templates with a specific design. Indeed, the geometrical features of the pores will be highly affected by parameters such as temperature, voltage, concentration and type of electrolyte, and even the stirring of the electrolyte during the process. The main features that describe a PAA template are the diameter of the pores, their height, the interpore distance, the thickness of the barrier layer, but also the ordering of the pores.

Approaching the perfect hexagonally-packed arrangement

Once the growth has started, the pores appear to grow perpendicular to the surface (we will use the general term "vertical" in the following), though nothing could have led to believe they would grow this way at the beginning of the anodization. Indeed, the initial growth direction of the pores mainly depends on the local orientation of the oxide/electrolyte interface, induced by the mechanical stress inside the alumina layer (see above). To explain the vertical and equidistant arrangement of the pores, it is suggested that the repulsive forces existing between neighouring pores, caused by mechanical stress, apply uniformly in pore bottom, creating an isotropic lateral stress that spreads pores homogeneously. Thus the alumina walls are pushed upwards, since the vertical direction is the only way for the material to expand [16]. It can clearly be seen on a cross-section of a PAA that the pore orientation is initially random and that they self-arrange as they penetrate the sample. For energy minimization reasons, a hexagonal structure forms on well-arranged samples, which can be found in many occasions in the nature, like in honeycombs, hexagonal basaltic columns, dried clay... (see Figure 1.2).

Figure 1.2: Examples of natural hexagonal arrangement in (a) honeycomb, (b) basaltic columns and (c) dried clay. (d) illustrates the formula below.

However, the conditions to obtain well-ordered, hexagonally-packed pores cannot be

arbitrarily chosen. Nielsch et al. [17] noticed that the porosity of a hexagonally-packed structure, defined as

$$P = \frac{2\pi}{\sqrt{3}} \times \left(\frac{r}{d_{int}}\right)^2$$

(where r is the pore radius and d_{int} the interpore distance, see Figure 1.2(d)), always takes values around 0.1 in the case of a well-defined self-ordered porous alumina. Connecting the applied potential U to the porosity thanks to $d_{int} = kU$:

$$U = \sqrt{\frac{2\pi}{\sqrt{3}P}}\frac{r}{k}$$

they showed that for a given pore diameter and respecting what they called the 10 % porosity rule, a unique, ideal value of U can be calculated and should be applied to get a perfect hexagonally-packed structure in the suitable acid electrolyte. They also measured the expansion volume (given by $\xi = \frac{V_{Alox}}{V_{Al}}$, with $1 < \xi < 2$), and brought out three cases. If $\xi \approx 1.2$, a good ordering is possible, but if $\xi < 1.2$, then the pore array remains disordered and if $1.3 < \xi < 2$ the higher ξ the smaller the size of ordered domains. The electrolyte has to be carefully chosen, as well as its concentration since the lower the pH (directly related to the concentration), the easier the field-enhanced dissolution. Thus, an adapted voltage range has been determined for several acid electrolytes [13], [18], such as sulfuric acid, oxalic acid, and phosphoric acid, which are the most common ones. These results are valid for the type of anodization called "mild anodization" (MA), in which current density is seldom higher than 10 mA.cm^{-2}. However, new self-ordering regimes have been discovered and allowed to extend the ranges that provide well-ordered pores. Basically, these regimes use higher current densities than for mild anodization (>100 mA.cm^{-2}) and correspond to the hard anodization (HA) process [19]. Like for MA, the interpore distance and the pore diameter are linearly proportional to the anodization voltage, but they found a porosity three times lower (3.3 %) than for MA. The advantage of using HA is a shorter fabrication time, since the pore growth rate is highly increased compared to MA. However, the high current density can damage the sample by causing a burning of the alumina film, which requires an appropriate cooling system. Kashi et al. [20] also developed what they called the "accelerated mild anodization", which provides a higher growth rate than MA, with similar r and d_{int}.

Of course temperature influences the ordering of the pores and the growth rate of the alumina [21]: the lower the temperature, the lower the growth rate. A different range of temperature giving the best ordering exists for each type of electrolyte. For example, the anodization in phosphoric acid is usually performed at 0-2°C, in order to prevent the sample from burning because of too high voltage (usually around 195 V).

The pore diameter and the interpore distance

It is well-known for decades that the pore diameter $d = 2r$ and the interpore distance d_{int} are directly related to the applied voltage U as follows: $d = k_1.U$, $d_{int} = k_2.U$, where $0.4 < k_1 < 0.9$ nm.V^{-1} and $k_2 \approx 2.5$-2.8 nm.V^{-1}, if the electrolyte is used in line with the

chosen voltage (see previous paragraph) [2], [13]. These values are approximative since they can vary with temperature and electrolyte concentration. An increasing temperature leads to an increasing pore diameter (it is typically varied between 0 and 30°C), whereas the interpore distance is not affected. An increasing electrolyte concentration also leads to a larger pore diameter, but slightly decreases the interpore distance. Choosing the appropriate electrolyte (see above), one can thus fabricate well-ordered PAA templates with a given interpore distance and pore diameter, adapting the anodization voltage. For example Zhang et al. got some pores 19 nm in diameter using 18 V in 10 wt% sulfuric acid [22], Ono and Masuko obtained some pores 34 nm in diameter with 40 V in 0.3 M oxalic acid [23], while Martin et al. fabricated large pores (up to 400 nm in diameter) with 195 V in 1 wt% phosphoric acid [24]. With the aim of reducing as much as possible the nano-devices that could provide the use of PAA, one can hope for a structure with ultra-thin pores. Beyond the classical electrolytes mentioned above, an optimized mix of several acids can allow the use of very low voltages, which could lead to very small pores (a few nanometers). Indeed, we have seen that the pore diameter is directly linked to the applied voltage, but not any electrolyte is appropriate for any voltage. By combining strong acids mix (H_2SO_4, HCl) and low voltage, Marquardt [25] managed to find an equilibrium between alumina dissolution and formation in these conditions, and realized PAA templates with pore diameter as small as 4 nm.

Non-straight pores

When 1D nanostructures with a special design are required, an interesting anodization technique provides pores with a modulated diameter, which can lead to nanowires with a varying diameter if a subsequent growth is performed. This technique simply consists in changing the applied voltage while the anodization is performed, which will change the pore diameter. This change has to be carried out carefully, since the equilibrium between the formation and the dissolution of alumina has to be preserved. Sulka et al. used a "pulse anodization" [26], which consists in applying a short "high" voltage (35 V) pulse to create hard anodization conditions between longer times at a lower voltage (25 V), which corresponds to mild anodization conditions. Comparable results were given in [27], where HA and MA processes have been alternated. Bodepudi et al. propose two methods to modulate the diameter of the pores [28]. A change in current density at a constant voltage can also modify the pore diameter, but they also use a simple pore widening process between two anodization steps in order to get a layer with large pores above a layer with narrow pores. These methods can be useful for various applications, such as magnetism of nanostructures [29] or to study in what extent the electrical and optical properties of diameter-modulated can differ from straight nanowires.

In the same vein of controlling the shape of the pores to grow nanostructures with special features, one can realize branched pores, from "Y-junctions" to complete tree-like porous alumina. The corresponding nanostructures grown inside are expected to exhibit novel properties, and could be used as building blocks as basic connectors in nanoelectronic devices. Y-junctions have been realized by abruptly increasing the anodization voltage, leading to a top-layer with vertical pores that split, forming two thinner pores

in an underlayer [30]. As a following, carbon nanotubes [31], metallic nanowires or even heterojunctions between NWs and NTs have been synthesized [32]. More complex structures, namely tree-like pores, have been fabricated in several ways. Cheng et al. used an exponential decrease technique, where the non-steady-state anodization has the effect of splitting the pores randomly [33], whereas symmetrical, tiered structure has been realized by a multiple step anodization, where both voltage and electrolyte were changed [34]. More anarchic, divided pores have been obtained by using Al substrates with special geometric features [35]. Nanopores were found to merge and to get curved on some specific areas of the sample, because of the non-homogeneous stress and electric field along the alumina.

The pore height

The height (or thickness) of the porous structure can be very easily tuned since it only depends on the duration of the anodization (for given conditions). Nevertheless the formation rate, which links the anodization duration to the height of the PAA, depends on numerous parameters such as the temperature (increases with T), the electrolyte and its concentration (increases with C), the applied voltage (increases with U), and what is called the dipping time (whose influence upon the formation rate depends on the temperature of the electrolyte) in [25]. Some research teams fabricated PAA templates with very high aspect ratios (> 500), with a thickness of several tens of microns [20], [36], anodizing their samples for several hours. For example, Lee et al. obtained well-ordered pores 100 nm in diameter, with a height of 110 µm after a two-hour anodization [19] (note that in this example a relatively short anodization was enough because they use the hard anodization process).

In the next section, we will detail the experimental set-up that we used to fabricate our own PAA templates, and our investigations about the different parameters of the anodization process. The fabrication and optimization of such templates have already been partially studied by our team, this has therefore to be understood as a continuation of the progress accomplished before.

1.3 Results and discussion

1.3.1 The experimental set-up

All the experiments have been realized using silicon wafers (Si wafers) as supports. Some teams use high-purity aluminium sheets to study porous alumina formation [15], but in our case and with a view to fabricating electronic devices, Si wafers are perfectly appropriate. Two different sample holders have been designed, depending on the size of the sample to anodize, that is an entire 2" wafer or a 1x1 cm^2 sample. The main challenge has been to contact electrically the sample on the back side, while immersed inside the electrolyte.

The set-up dedicated to 2" wafers is composed of a glass electrolyte container ('a' in Figure 1.3(a)), with a wide circular aperture on the bottom. Once the sample is mounted

as shown in Figure 1.3(a), the container is put on the sample so that, once filled, the electrolyte covers it. The leakages are prevented thanks to an o-ring ('b' in Figure 1.3(a)) which is the size of the aperture ($\approx$ 11 cm^2) and a pressure applied on the electrolyte container by four screws ('c' in Figure 1.3(a)) and two steel plates ('d' in Figure 1.3(a)). Since these plates are conductive, the bottom one is used as a back contact to the sample for the anodization.

In case of smaller sample (1x1 cm^2), the other sample holder has to be used. Here the entire set-up is immersed inside the electrolyte, so a Teflon-based material has been chosen to fabricate every piece in contact with it, since it contains acid. First, the sample is mounted on a copper support with silver paste ('a' in Figure 1.3(b)). This copper support is pressed inside the Teflon holder ('b' in Figure 1.3(b)) against a little o-ring thanks to a steel screw ('c' in Figure 1.3(b)), and then locked inside the holder with a Teflon plate and three Teflon screws. Thus, once in the electrolyte, everything is insulated inside the sample holder except a small surface of the sample of about 0.29 cm^2 (see the little hole in 'b' in Figure 1.3(b)), which is covered by the electrolyte inside a beaker. The electrical contact is ensured by a steel rod ('d' in Figure 1.3(b)) that contacts the copper plate through the sample holder.

The final assembly, in the case of 2" wafers, is shown in Figure 1.3(c). The assembly for 1 cm^2 samples is very similar, and doesn't need to be described in detail. Once the sample is immersed in the electrolyte, in both cases a graphite counter-electrode ('a' in Figure 1.3(c)) is used as a cathode to perform the anodization, the anode being the sample itself. A glass stirrer ('c' in Figure 1.3(c)) is also used in both cases to prevent local heating in the electrolyte, and ensure its homogeneity.

The anodizations were performed in the potentiostatic mode, thanks to a stabilized power supply, and the current was measured thanks to a Metrix multimeter, connected to a computer through its RS 232 output in order to visualize the current-time curve, generated by a home-made Labview program. As it has already been mentioned above, it is usually useful to perform the anodization at low temperature to get a better pore ordering. In that purpose a special glass coil ('b' in Figure 1.3(c)) was fabricated to cool down the electrolyte in the 2" type set-up, and a double-walled container was used to receive the electrolyte beaker for the 1 cm^2 sample set-up. Both devices were connected in serial to a thermoregulator using silicone oil as a thermofluid, which allows to carry out anodizations at temperatures as low as 1°C.

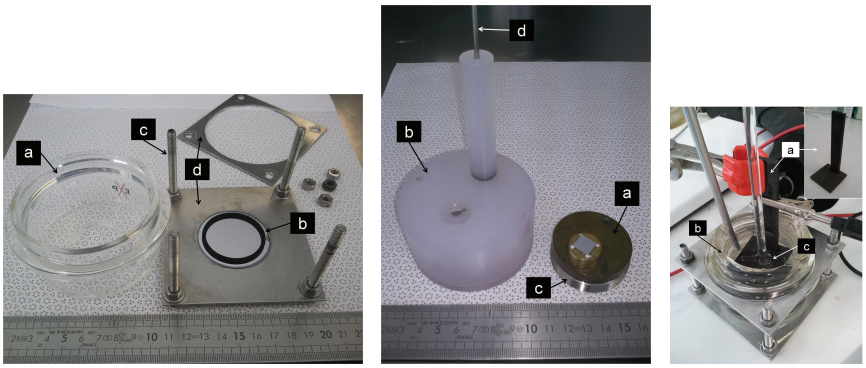

(a) (b) (c)

Figure 1.3: (a) Anodization setup for 2" wafers, (b) anodization setup for small samples (1 cm^2) and (c) anodization setup for 2" wafers, with graphite cathode (a), glass coil cooler (b), and glass stirrer (c).

1.3.2 The PAA template fabrication process

The following deals with the fabrication and the control of PAA films with desired features. We will talk about the two-step anodization process conditions, the growth rate of the pores, which is necessary to control the PAA thickness, then we will see how we can overcome the the problems related to the barrier layer, and finally the method we have used to fabricate through-hole PAA films on the Si substrates.

The two-step anodization

All the anodization steps have been carried out the same way. First of all an Al layer is deposited by evaporation on 2" (100) Si wafers, in an e-beam evaporator. The Si wafers are beforehand sonicated successively in acetone and propanol, then rinsed in DI water and dried under N_2, in order to make the interface between Al and Si as clean and as flat as possible. Indeed, a non flat interface would lead to a non-homogeneous Al layer, which then would give an alumina porous layer with a non homogeneous thickness. In some cases, in order to get a perfectly-cleaned surface, an RCA-like treatment is even performed, especially when we plan to carry out the entire process until an electronic device. Depending on the desired height of the future alumina, a more or less thick layer is deposited. The pressure inside the evaporation chamber is decreased down to a few 10^{-7} Torr, and the current passing through the crucible is around 0.50 A, which deposits Al with a rate of ≈ 0.5 nm.s^{-1}. Note that such a low pressure and a highly-pure Al target are essential, since a low purity of the deposited Al would lead to a very bad formation of porous alumina. As an illustration, we couldn't manage to fabricate a proper PAA from a target containing as little as 0.5 % of incorporated copper (this composition may be useful for other applications). We suggest that the few Cu atoms prevent the Al from being oxidized properly by modifying the exchange events that occur in pure Al.

In most cases the two-step method (see 1.1, p.7)) has been performed in order to get

a good ordering on the top of the PAA. Basically it consists in anodizing a sacrificial Al layer (first step), removing it, and then anodizing the remaining Al again (second step). Indeed, we realized that the pores were rather straight and well ordered as soon as the first anodization, but that the top of the PAA was inevitably disordered, because of the preliminary period when the pores get organized at the beginning of the anodization process (see below). Then the rest of the membrane is straighter, which corresponds to the steady state, when pores grow parallel towards the bottom of the sample. For this reason we performed a first anodization, which led to a temporary porous membrane, which has the effect to create some ordered, scalloped pore prints on the surface of the underlying Al layer. When this temporary membrane is chemically removed (we used a typical mixture of 0.2 M CrO_3 and 0.6 M H_3PO_4 for 40 min at 60°C), the Al layer surface is "pre-patterned", that is to say that the individual paths mentioned in 1.2.2 will preferentially form in these ordered nano-prints, which will lead to the formation of well-ordered vertical pores as soon as the second anodization begins. The pores are therefore completely straight all along the membrane (Figure 1.4(a)), which is of high interest for further dry etching (see chapter 4). Depending on the pore diameter required (1.2.3), we applied either 20 V in a 0.3 M H_2SO_4 solution, or 40 V in a 0.3 M oxalic acid solution, which are the common anodization conditions. We seldom used higher voltages, since current instability and overheating problems easily take place in this case. Besides our goal is not to fabricate large pores. In Figure 1.4(a), the pore diameter is between 28 and 40 nm and the interpore distance (top view not shown here) about 102 nm, which corresponds to k_1 = 0.7-1.0 nm.V^{-1} and $k_2 \approx 2.55$ nm.V^{-1}, which is good accordance with the k_1 and k_2 values given in p.1.2.3.

For the sake of reproducibility, these two steps have to be performed the same way from one sample to another, especially concerning the time the sample is immersed inside the electrolyte before the anodization. Marquardt showed that this "dipping time" is a crucial parameter regarding the growth rate [25], this is why a constant time (between 15 and 20 min, corresponding to the time needed for the temperature to decrease again after the immersion of the sample) was respected between the immersion of the sample and its anodization. The two-step method is simple, cheap and therefore widely used by research teams who work on PAA; nevertheless an alternative method, called the molding process, can also provide highly-ordered porous templates. Basically it consists in creating the same kind of prints as the ones created by the first anodization, but using a solid mold whose convex prints are pressed against the Al sample [5]. Then the anodization is performed classically from the patterned sample.

Figure 1.4(b) shows the beginning of the I(t) curves of the first anodization (FA) and the second anodization (SA), respectively. Two main differences between the two curves can be noticed. First, the minimum current (stage II in Figure 1.1) is always reached sooner for the SA than for the FA. Secondly, this minimum is markedly higher than the FA one, as well as the steady state current. The first difference can be explained by the nano-prints made during the FA, which make the individual formation (see 1.2.2, p.9) quite easier. The initiation of the pore growth is therefore brought forward, since the pores are almost "ready to grow". If the SA curve is usually above the FA one, this is due

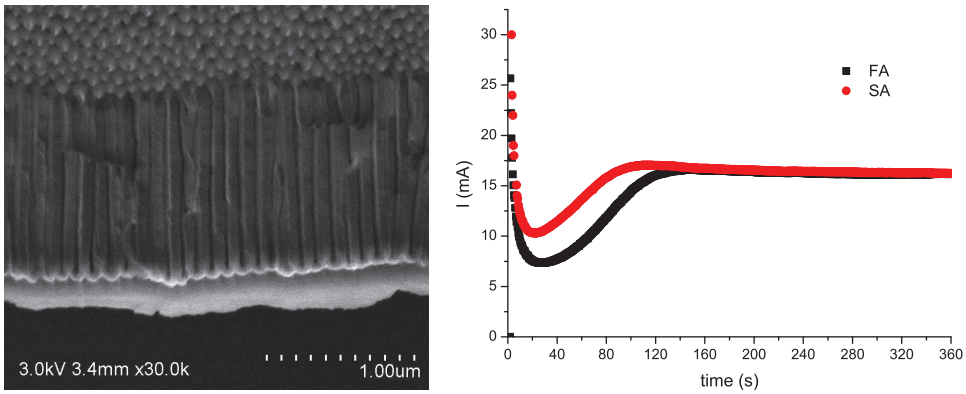

(a) (b)

Figure 1.4: (a) SEM cross-section picture of a PAA template after the second anodization and (b) corresponding FA and SA current-time curves.

to practical reasons. As mentioned in section 1.2.2, a lot of Al^{3+} ions are extracted from both Al and Al_2O_3 and dissolved inside the electrolyte. If the same electrolyte is then used to perform the SA, its chemical composition is different compared to the one used for the FA. Since the current measured is mostly ionic, Al^{3+} ions from FA contribute to increase the current during the SA.

Adjusting the pore diameter

As already explained in p.12, the higher the anodization voltage, the wider the pores. As an illustration we performed three anodizations at different voltages, i.e. at 20 V, 40 V and 140 V, respectively. Of course the electrolyte has been adjusted in each case in order to get a good pore ordering, as mentioned in p.12. We chose sulfuric acid, oxalic acid, and phosphoric acid, respectively, each with a 0.3 M concentration. The results are visible in Figure 1.5.

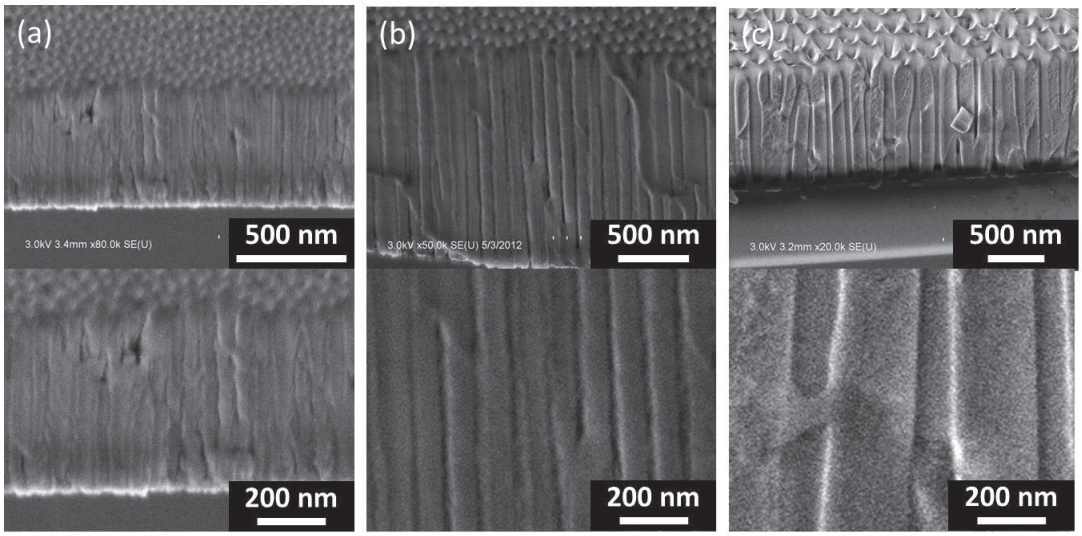

Figure 1.5: SEM cross-sections of PAA anodized at (a) 20 V in sulfuric acid, (b) 40 V in oxalic acid and (c) 140 V in phosphoric acid. The bottom pictures are magnifications from the top ones at the same scale, in order to compare the size of the pores.

The pore diameter varies between ≈ 10-15 nm for the anodization at 20 V, up to almost 200 nm for the anodization at 140 V. One can notice that the anodization duration differed between each of the pictures shown here (respectively 10 min, 30 min and 1h15) but that this only impacts the pore height and not the pore diameter at all. An interesting thing to notice as well is the increasing thickness of the pore walls with the increasing voltage. This is all the more visible in the bottom pictures, where the scale hadn't been adjusted to fit the page: the pores formed at 140 V are amazingly larger than those formed at 20 V.

Adjusting the PAA thickness

Depending on the subsequent experiments one wants to perform, it is capital to control the height of the vertical pores of the PAA template. If long nanostructure growth is required, of course a thick PAA will be fabricated to receive the whole length in the pores, and to keep nanostructures from protruding out of the membrane. On the contrary, it would be a waste of time to fabricate a too thick membrane if small structures or even particles are deposited. Furthermore, a too thick membrane can lead to a bad pore filling, and make a pattern transfer more difficult [37]. It is therefore of high interest to calibrate the growth rate of PAA, and this for every anodization conditions. As a basic example, we carried out a small serie of experiments to show in what extent the thickness of a PAA can vary. We anodized Al layers in two steps at 20 V in 0.3 M sulfuric acid, with different second anodization durations. As we could expect, the longer the anodization the thicker the PAA layer (i.e the highest the pores), as shown by the graph in Figure 1.6. This led to PAA 150 nm to 1.2 µm in thickness for 2 min and 28 min anodization, respectively. One can notice the two different slopes of the fitting linear

curves, corresponding to growth rates of $\approx$ 104 nm.min^{-1} and 29 nm.min^{-1}. We didn't expect such a high slowing down during the anodization process, but we attribute it to the increasing pore depth, which makes the ion transport harder as the pores become higher. Three cross-sections are presented as an illustration in Figure 1.7. Such a study is important to calibrate the PAA growth rate, since the majority of the subsequent experiments will be carried out under these conditions.

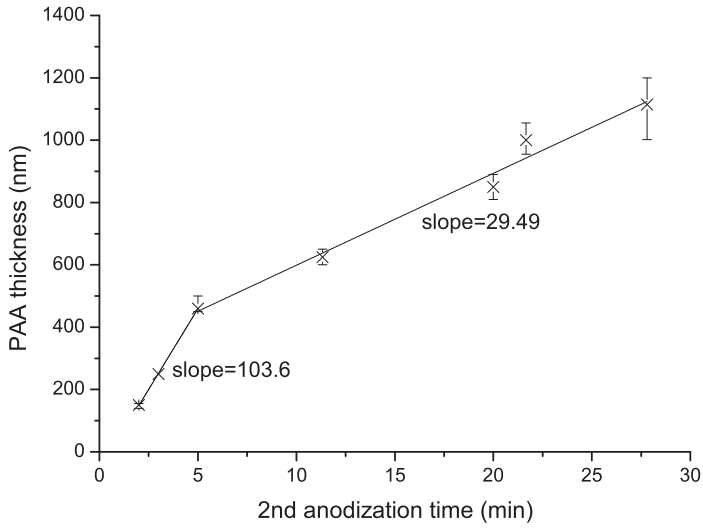

Figure 1.6: Thickness of PAA as a function of the second anodization time. The sample was anodized under 20 V in 0.3 M sulfuric acid.

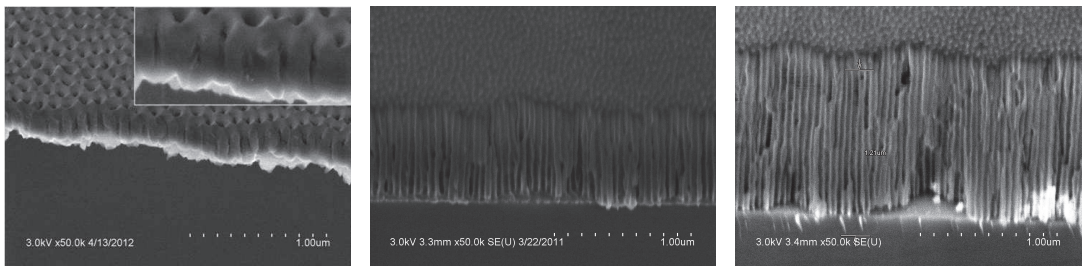

(a) (b) (c)

Figure 1.7: Cross-section of PAA templates after a second anodization of (a) 2 min, (b) 11 min and (c) 28 min. The three samples are magnified 50 000 times, the inset in (a) is a 100,000x magnification.

Some applications may need a given thickness of non-oxidized aluminium (including no Al at all) under the PAA. To do so, the two-step anodization appears more complex

than it seems, since both first and second anodization duration have to be calibrated. Indeed, the first anodization determines how much Al will remain after the temporary PAA removal (1.3.2), which will impact the thickness of the remaining Al under the final PAA, after the second anodization. For example, if no Al is needed under the final PAA, one should know exactly how much Al is needed to lead to the correct thickness of porous alumina, taking the volume expansion into account (1.2.2). Therefore one should beforehand anticipate how much non-oxidized Al will be available after the first anodization.

At the end of the second anodization, if Al is not completely consumed, then the oxide layer which ions used to travel through during the anodization is still visible (Figure 1.4(a)). This oxide layer is commonly called the barrier layer. It could be useful if an effective insulator between the interior of the pores and the substrate is needed, but its presence is not desired if one wants to use the PAA as an etching mask or if an electrical contact is needed between nano-objects grown inside the pores and the underlying layer. The next paragraph deals with different methods to get rid of this barrier layer.

The barrier layer etching

The back access to the nanostructures grown inside PAA templates is hindered by the barrier layer, therefore a through-hole structure is required for a lot a applications. Several techniques have been developed, like ion milling [38], plasma etching [39], and wet etching [5]. The latter has been widely used, included in our studies, and consists in using an acidic solution (typically phosphoric acid) to chemically etch the oxide barrier layer at the bottom of the pores. This method is very simple, but has some drawbacks related to its isotropy. Indeed, when the sample is immersed, the barrier layer is etched by the H_3PO_4, but the pore walls as well, they are therefore progressively thinned. Han et al. [40] reported that though pore walls and barrier layer are both basically made of alumina, their composition might slightly change, since barrier layer sees many damaging events during the anodization, like atoms incorporations, dissolving, ions travelling..., which weakens its structure and leads to a less dense material. Therefore their density and reactivity towards phosphoric acid might be different, and the etching rate of pore walls should be lower than the one of the barrier layer. A simple study of the barrier layer thickness of a sample immersed in phosphoric acid for different times allows to determine the etching rate of the barrier layer. For this study we anodized a sample for 3 min (for the second anodization) in 0.3 M oxalic acid at 40 V and 5°C, which gave a 250 nm thick PAA with pores 20 nm in diameter. The barrier has an average thickness of 60 nm before any etching. We immersed this PAA in a 0.3 M H_3PO_4 solution at 30°C for several durations, and reported the barrier layer thickness, measured on the SEM pictures, as a function of the immersion time on Figure 1.8. Some SEM micrographs are also visible in Figure 1.9.

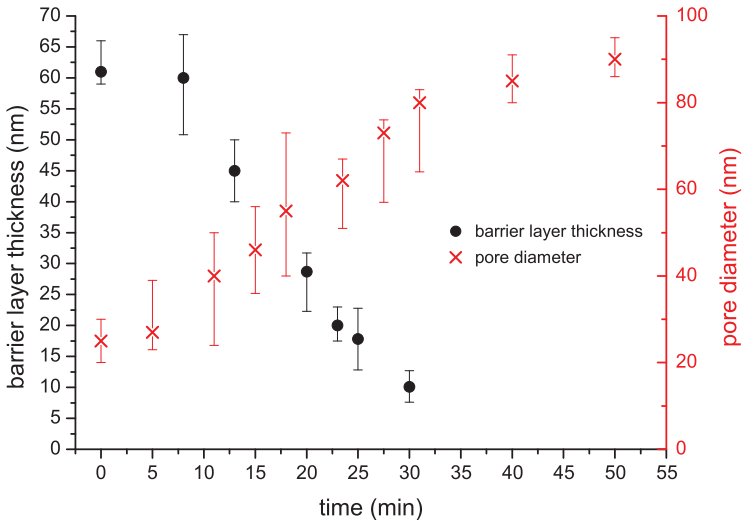

Figure 1.8: Barrier layer thickness (black circles) and pore diameter (red crosses) as a function of the immersion time in H_3PO_4. Anodization took place in oxalic acid at 40 V.

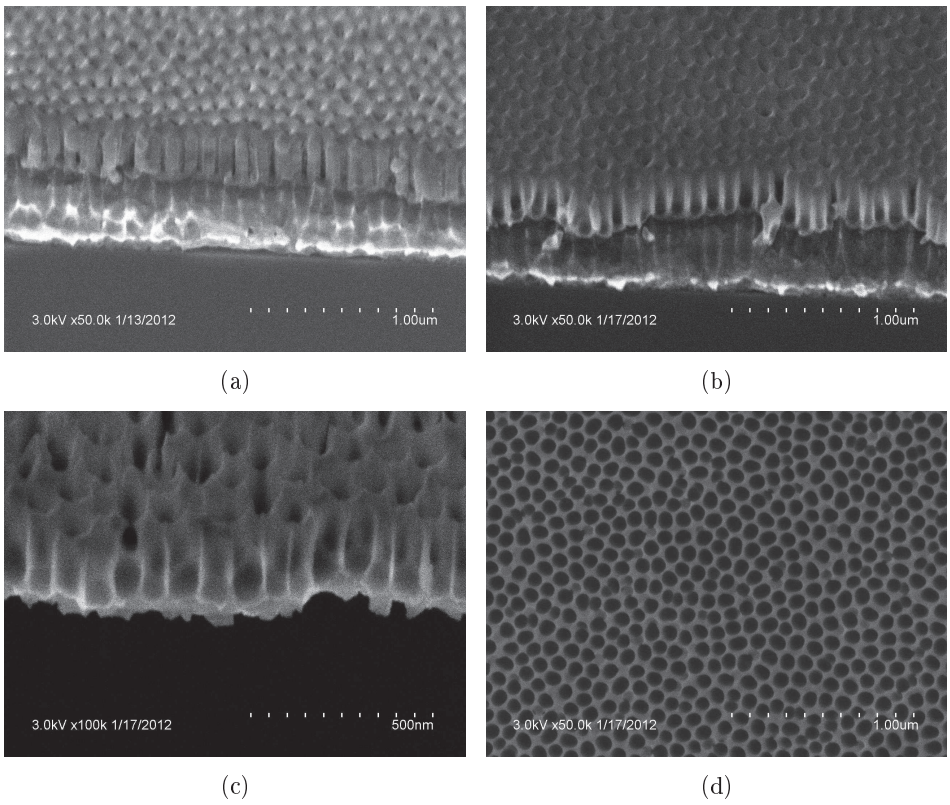

Figure 1.9: PAA after second anodization (3 min), (a) before the pore widening process, (b) and (c) after a 20 min and 30 min pore widening process, respectively. (d) is the corresponding top-view of (c).

Even for long etchings (here the maximum we performed was 30 min), a thin barrier layer (about 10 nm) is still present. The problem is that even if the barrier layer is sufficiently thinned, the pore walls have become very thin (see Figure 1.11(c)), and therefore the pore diameter has increased (see Figure 1.8). Such a long etching carries the risk to highly weaken the porous structure, or even to destroy it. Nevertheless, the top-view presented in 1.11(d) shows that the pores have not merged yet, and that the porous structure is still usable in that extreme case. For this reason, it is also important to know the evolution of the pore diameter as a function of the immersion time.

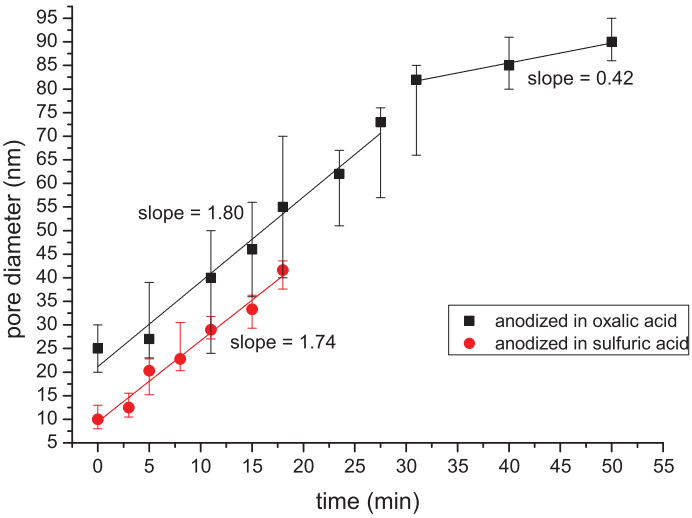

Figure 1.10: Pore diameter as a function of the pore widening duration, for samples anodized in oxalic acid (black squares) and in sulfuric acid (red circles).

We therefore studied more deeply the pore walls etching, by immersing some samples in the same H_3PO_4 solution for different durations. This operation can be used to adjust the pore diameter to a desired value, and is therefore often called "pore widening". We can see on both curves in Figure 1.10, corresponding to samples anodized in oxalic acid and in sulfuric acid, respectively, that the pore diameter increases linearly with the duration of immersion, at least at the beginning of the etching. We have found comparable etching rates for both kinds of samples: the pore walls were found to be etched at ≈ 1.80 nm.min^{-1} for the sample anodized in oxalic acid, and at ≈ 1.74 nm.min^{-1} for the sample anodized in sulfuric acid. The curve of the sample anodized in oxalic acid shows that the etching rate markedly decreases after 30 minutes of etching, down to ≈ 0.42 nm/min for longer etchings. Instead of continuing with the same etching rate until the complete dissolution of the PAA, it seems like the pore walls become harder to etch as they get thinner, delaying their complete dissolution. Indeed, according to the average interpore distance estimated to 95 nm, the maximum pore diameter (i.e

corresponding to a theoretical pore wall thickness of 0 nm) should be reached after a 41 min etching (by extrapolating the first part of the curve), and yet we still can see pore walls after a 50 min etching (though ultra-thin). This phenomenon has already been reported and can be explained by the existence of two regions of a different structure in the pore walls. Indeed, as noticed by Thompson and Wood [41], the difference in mobility of the oxalate ions ($C_2O_4^{2-}$) and the oxygen ions in alumina leads to the inner wall being more contaminated by oxalate ions than the outer wall, thus creating different densities in the pore walls (Figure 1.12). This results in the inner layer being more easily etched than the outer layer, which is composed of non-contaminated alumina (almost pure), and thus to a variation of the etching rate, occurring when the inner layer is completely removed (see also [40]). However, this has not been observed for PAA films fabricated in sulfuric acid, probably due to the very thin pore walls in which the two layers mentioned in Figure 1.12 may not be so distinct.

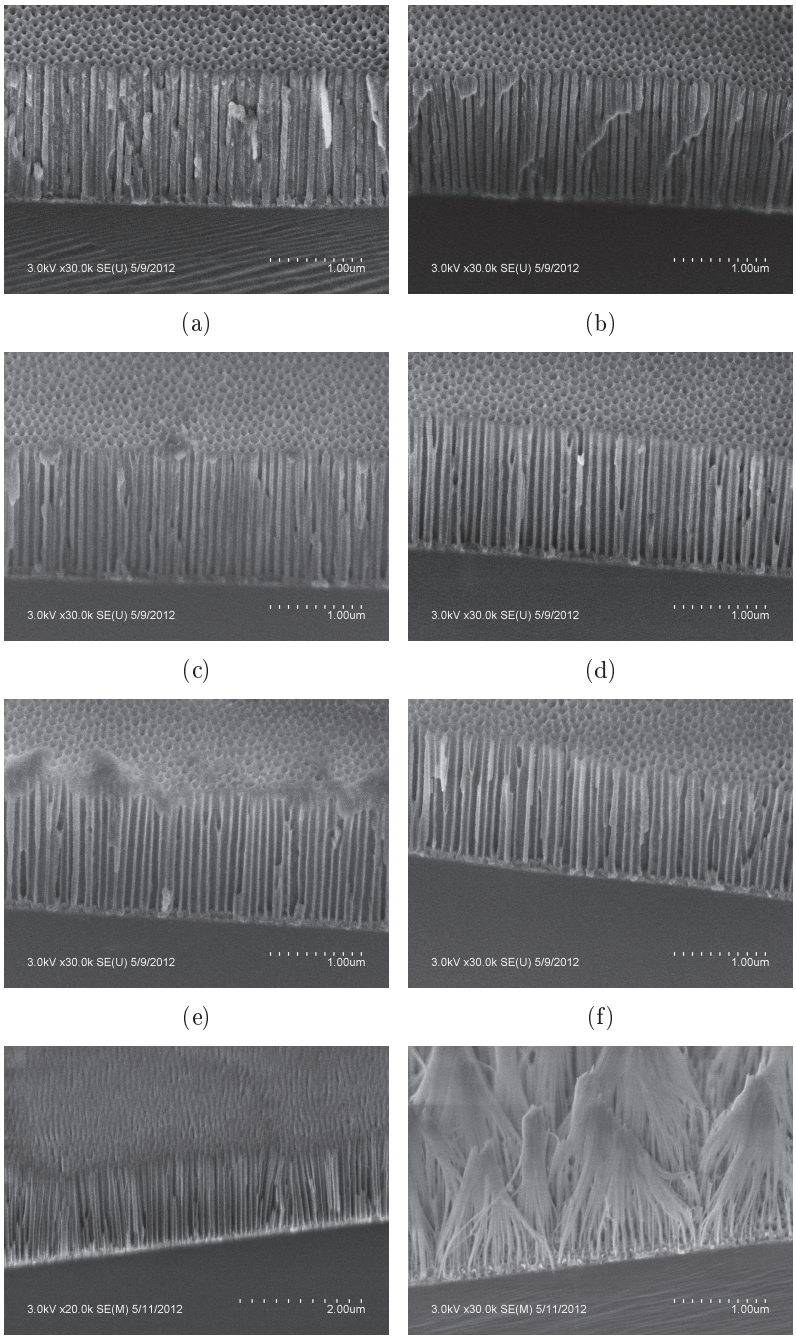

Figure 1.11: Evolution of the pore diameter after immersion in 0.3M H_3PO_4 for (a) 5 min, (b) 11 min, (c) 18 min, (d) 23 min 30 sec, (e) 27 min 30 sec, (f) 31 min, (g) 40 min 30 sec and (h) 50 min.

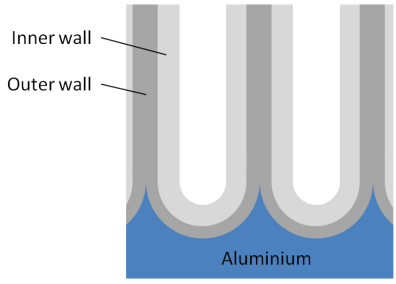

Figure 1.12: Schematic drawing of the bi-layer structure of the pore walls. The inner wall is oxalate ions-contaminated, and the outer wall is purer alumina.

The pore widening is a fast, simple method to decrease the thickness of the barrier layer, but is not appropriate if one doesn't want the template pores to get wider. Another way to etch this barrier layer would be to use a reactive plasma, which can provide a high etching anisotropy thanks to the bombarding effect. Nevertheless alumina is known to be one the hardest material to etch, and a thickness as low as several tens of nanometers would take several minutes to etch, which would damage the sample more than it would etch the barrier. Therefore a combination of those two methods could be useful if a sufficiently thin barrier layer would remain, and if the pore walls are already too thin to continue the pore widening. A short, highly anisotropic etching would then be enough to etch the thin barrier layer without bombarding the rest of the sample too much. This method will be discussed in chapter 4; however, the pore widening process still lacks homogeneity, since the thickness of the barrier layer can slightly vary from one pore to another.

A classier, easier method to thin down the barrier layer consists in progressively decrease the anodization voltage at the end of the anodization. Indeed, as well as for the pore diameter, the barrier layer thickness d_{bl} happens to depend on the anodization voltage U: $d_{bl} = k.U$, where k is a constant depending on the anodization conditions. Each time a new voltage is applied, a new equilibrium between alumina dissolution and formation self-adjusts, leading to a branched structure after several decrease steps [33]. Based on this method, a precise control has been developed by Marquardt et al., consisting in a continuous exponential voltage decrease, and leading to a slightly-branched structure, with efficiently thinned barrier layer at the bottom of the pores [42]. A simple subsequent pore widening can then be used to completely remove the remaining barrier layer.

For the simplicity that it provides, the wet etching of the barrier layer has been chosen for the following, and especially for the study of the Al etching discussed in chapter 4. However, a last method is described in the next paragraph, and explains how to fabricate vertical pores on Si without barrier layer.

Open pores on silicon

When no Al is needed beneath the PAA, one can perform its complete anodization, which leads to a barrier-free PAA standing on a Si substrate. The advantage is that one no longer has to remove the alumina barrier layer and that the back access to the nanostructures inside the pores is therefore made easier. The process is as follows: when the Al layer is completely oxidized, the remaining barrier layer is dissolved with the help of the electric field in the same way as during the rest of the anodization, until it completely disappears and leaves through-hole pores. One can easily control this complete anodization by mastering the current-time curve (see Figure 1.13(a)).

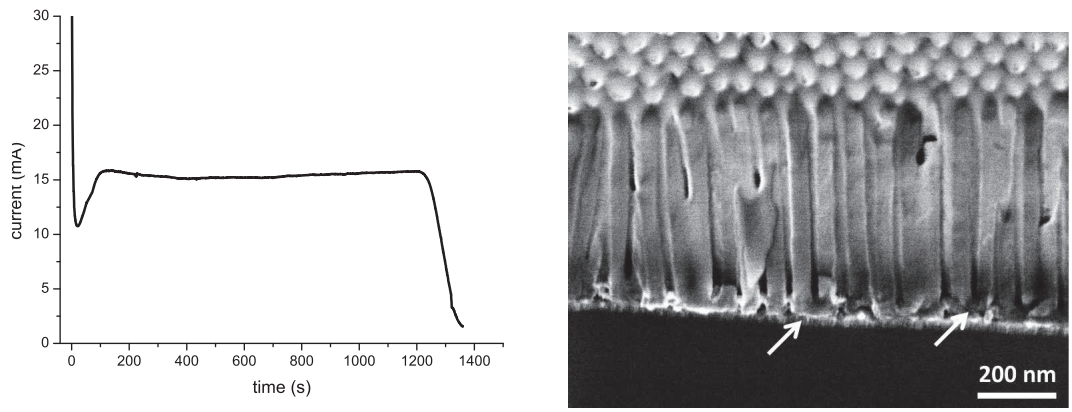

(a) (b)

Figure 1.13: (a) I(t) curve showing the current drop at the end of the anodization and (b) corresponding SEM cross-section.

At the end of the steady-state, an abrupt decrease occurs at the very moment when the last part of Al is consumed, that is when the bottom of the barrier layer reaches the Si surface. From this moment on, since there is no Al left on the sample, the current can only pass through silicon, which is more resistive, hence the current decrease. However, this decrease is not instantaneous, and can sometimes take several tens of seconds before it stabilizes. This is to be correlated to the inhomogeneity of the layer thickness: all the pores don't reach the Al/Si interface at the same time, therefore the Al disappearance is rather progressive, and the increase of the resistance too. Meanwhile, only the field-enhanced dissolution of alumina occurs, leading to immediate oxidation of the underlying material, that is silicon, as soon as the barrier layer is etched away. We will see later (chapter 3) that if the underlayer is hardly or non-oxidable, like gold, the current dramatically increases after the steady state, for the same reasons. In case of PAA realized on Si, one must be careful not to create another barrier oxide, namely silicon oxide, after the current decrease. The anodization has to be stopped at a precise moment, that is exactly after the barrier layer removal and before the silicon oxidation. This is a bit tricky, and it has been shown [25] that stopping the anodization as soon

as the current reaches a certain percentage of the steady state current ($\approx$ 30 %) was enough to get open pores. This value has to be calibrated for every condition, and is visible on the current-time curve, when the decrease becomes slower (from 1300 s in Figure 1.13(a)). If one waits a longer time, the underlayer may well be oxidized and if the anodization is stopped earlier, some pores must remain close. In the example that follows, we stopped the anodization when I = 40 % I_p, where I_p is the current at the plateau of the I(t) curve. It appears in Figure 1.13(b) that the main part of the pores are opened, but a few pores (white arrows) still exhibit a small barrier layer, which reveal the inhomogeneity of the thickness of the barrier layer during the anodization.

Table 1.1 sums up the different anodization and etching conditions we performed in this chapter.

Electrolyte	Sulfuric acid	Oxalic acid	Phosphoric acid
Voltage (V)	20	40	140
Pore diameter (nm)	9.2-14.8	28-40	120-182
Growth rate (nm.min^{-1})	29-104	$\approx$ 50-55	33-50

Table 1.1: Summary table of the anodization and etching conditions.

1.4 Conclusion

The principles and the motivations of the realization of a Porous Anodic Alumina (PAA) layer have been presented, with some details concerning the chemistry and the physics occurring during its formation. Basing on the state of the art and on our own investigations, we explained how to play on the different experiment conditions to customize the features of the PAA. We especially focus on how to get large arrays of well-ordered vertical pores. The influence of the applied voltage, the composition of the electrolyte, the duration of the anodization, the temperature, and other parameters has been discussed. The interest of performing the anodization of aluminium in two steps has been shown and the problem of the alumina barrier layer has been dealt with, while giving several ways to remove it. Particularly, we focused on the fabrication of through-hole pores standing on silicon substrate, which fabrication requires a calibration to prevent the oxidation of the substrate.

These results constitute an important basis for further investigations, like the guided growth of nanostructures inside vertical pores. For this purpose, several studies have been carried out from the results of this chapter. One is the use of a PAA template as a hard mask to realize anisotropic etchings and will be presented later on. The other one is the deposition of metallic catalysts at the bottom of the pores of a PAA template, which implies the fabrication of vertical pores on a silicon substrate, already seen in this chapter. This is the topic of the second chapter. The geometrical features of the PAA being directly linked to the shape and the density of the latter, their control is therefore of high interest.

Bibliography

[1] F. Keller, M. S. Hunter, and D. L. Robinson, "Structural features of oxide coatings on aluminum," *Journal of The Electrochemical Society*, vol. 100, no. 9, pp. 411–419, 1953.

[2] J. P. O'Sullivan and G. C. Wood, "The morphology and mechanism of formation of porous anodic films on aluminium," *Proceedings of the Royal Society of London. A. Mathematical and Physical Sciences*, vol. 317, pp. 511–543, July 1970.

[3] Y. Xu, G. Thompson, G. Wood, and B. Bethune, "Anion incorporation and migration during barrier film formation on aluminium," *Corrosion Science*, vol. 27, no. 1, pp. 83–102, 1987.

[4] H. Masuda and K. Fukuda, "Ordered metal nanohole arrays made by a two-step replication of honeycomb structures of anodic alumina," *Science*, vol. 268, pp. 1466–1468, June 1995.

[5] H. Masuda, H. Yamada, M. Satoh, H. Asoh, M. Nakao, and T. Tamamura, "Highly ordered nanochannel-array architecture in anodic alumina," *Applied Physics Letters*, vol. 71, pp. 2770–2772, Nov. 1997.

[6] D. Gong, C. A. Grimes, O. K. Varghese, W. Hu, R. S. Singh, Z. Chen, and E. C. Dickey, "Titanium oxide nanotube arrays prepared by anodic oxidation," *Journal of Materials Research*, vol. 16, no. 12, pp. 3331–3334, 2001.

[7] N. Mukherjee, M. Paulose, O. K. Varghese, G. K. Mor, and C. A. Grimes, "Fabrication of nanoporous tungsten oxide by galvanostatic anodization," *Journal of materials research*, vol. 18, no. 10, pp. 2296–2299, 2003.

[8] I. Sieber, B. Kannan, and P. Schmuki, "Self-assembled porous tantalum oxide prepared in H2SO4/HF electrolytes," *Electrochemical and Solid-State Letters*, vol. 8, no. 3, p. J10, 2005.

[9] H. Tsuchiya, J. Macak, I. Sieber, and P. Schmuki, "SelfOrganized HighAspectRatio nanoporous zirconium oxides prepared by electrochemical anodization," *Small*, vol. 1, pp. 722–725, July 2005.

[10] Z. Su and W. Zhou, "Formation mechanism of porous anodic aluminium and titanium oxides," *Advanced Materials*, vol. 20, pp. 3663–3667, Oct. 2008.

[11] F. Li, L. Zhang, and R. M. Metzger, "On the growth of highly ordered pores in anodized aluminum oxide," *Chem. Mater.*, vol. 10, no. 9, pp. 2470–2480, 1998.

[12] V. P. Parkhutik and V. I. Shershulsky, "Theoretical modelling of porous oxide growth on aluminium," *Journal of Physics D: Applied Physics*, vol. 25, pp. 1258–1263, Aug. 1992.

[13] A. P. Li, F. Muller, A. Birner, K. Nielsch, and U. Gosele, "Hexagonal pore arrays with a 50–420 nm interpore distance formed by self-organization in anodic alumina," *Journal of Applied Physics*, vol. 84, no. 11, p. 6023, 1998.

[14] S. J. Garcia-Vergara, L. Iglesias-Rubianes, C. E. Blanco-Pinzon, P. Skeldon, G. E. Thompson, and P. Campestrini, "Mechanical instability and pore generation in anodic alumina," *Proceedings of the Royal Society A: Mathematical, Physical and Engineering Science*, vol. 462, pp. 2345–2358, Aug. 2006.

[15] G. D. Sulka and W. J. Stepniowski, "Structural features of self-organized nanopore arrays formed by anodization of aluminum in oxalic acid at relatively high temperatures," *Electrochimica Acta*, vol. 54, pp. 3683–3691, May 2009.

[16] O. Jessensky, F. Müller, and U. Gösele, "Self-organized formation of hexagonal pore arrays in anodic alumina," *Applied Physics Letters*, vol. 72, pp. 1173–1175, Mar. 1998.

[17] K. Nielsch, J. Choi, K. Schwirn, R. B. Wehrspohn, and U. Gösele, "Self-ordering regimes of porous alumina: the 10 porosity rule," *Nano Lett.*, vol. 2, no. 7, pp. 677–680, 2002.

[18] S. Ono, M. Saito, M. Ishiguro, and H. Asoh, "Controlling factor of self-ordering of anodic porous alumina," *Journal of The Electrochemical Society*, vol. 151, no. 8, pp. B473–B478, 2004.

[19] W. Lee, R. Ji, U. Gösele, and K. Nielsch, "Fast fabrication of long-range ordered porous alumina membranes by hard anodization," *Nature Materials*, vol. 5, pp. 741–747, Aug. 2006.

[20] M. A. Kashi, A. Ramazani, M. Raoufi, and A. Karimzadeh, "Self-ordering of anodic nanoporous alumina fabricated by accelerated mild anodization method," *Thin Solid Films*, vol. 518, pp. 6767–6772, Sept. 2010.

[21] M. A. Kashi and A. Ramazani, "The effect of temperature and concentration on the self-organized pore formation in anodic alumina," *Journal of Physics D: Applied Physics*, vol. 38, pp. 2396–2399, July 2005.

[22] F. Zhang, X. Liu, C. Pan, and J. Zhu, "Nano-porous anodic aluminium oxide membranes with 6–19 nm pore diameters formed by a low-potential anodizing process," *Nanotechnology*, vol. 18, p. 345302, Aug. 2007.

[23] S. Ono and N. Masuko, "Evaluation of pore diameter of anodic porous films formed on aluminum," *Surface and Coatings Technology*, vol. 169–170, pp. 139–142, June 2003.

[24] J. Martín, C. V. Manzano, and M. Martín-González, "In-depth study of self-ordered porous alumina in the 140–400 nm pore diameter range," *Microporous and Mesoporous Materials*, vol. 151, pp. 311–316, Mar. 2012.

[25] B. Marquardt, "Organisation nanometrique de composant (nanotubes de carbone) utilisant des membranes verticales d'alumine anodique poreuse." http://tel.archives-ouvertes.fr/index.php?halsid=pjkpepq00t6oqf5pbns4tj48j3&view_this_doc=pastel-00005877&version=1, Dec. 2009.

[26] G. D. Sulka, A. Brzózka, and L. Liu, "Fabrication of diameter-modulated and ultrathin porous nanowires in anodic aluminum oxide templates," *Electrochimica Acta*, vol. 56, pp. 4972–4979, May 2011.

[27] W. Lee, K. Schwirn, M. Steinhart, E. Pippel, R. Scholz, and U. G|[ouml]|sele, "Structural engineering of nanoporous anodic aluminium oxide by pulse anodization of aluminium," *Nature Nanotechnology*, vol. 3, pp. 234–239, Mar. 2008.

[28] S. C. Bodepudi, D. Bachman, and S. Pramanik, "Fabrication of highly ordered cylindrical nanopores with modulated diameter using anodic alumina," in *2011 International Conference on Nanoscience, Technology and Societal Implications (NSTSI)*, pp. 1–4, IEEE, Dec. 2011.

[29] K. Pitzschel, J. Bachmann, S. Martens, J. M. Montero-Moreno, J. Kimling, G. Meier, J. Escrig, K. Nielsch, and D. Gorlitz, "Magnetic reversal of cylindrical nickel nanowires with modulated diameters," *Journal of Applied Physics*, vol. 109, pp. 033907–033907–6, Feb. 2011.

[30] L.-B. Kong, "Synthesis of y-junction carbon nanotubes within porous anodic aluminum oxide template," *Solid State Communications*, vol. 133, pp. 527–529, Feb. 2005.

[31] J. Li, C. Papadopoulos, and J. Xu, "Nanoelectronics: Growing y-junction carbon nanotubes," *Nature*, vol. 402, pp. 253–254, Nov. 1999.

[32] G. Meng, F. Han, X. Zhao, B. Chen, D. Yang, J. Liu, Q. Xu, M. Kong, X. Zhu, Y. Jung, Y. Yang, Z. Chu, M. Ye, S. Kar, R. Vajtai, and P. Ajayan, "A general synthetic approach to interconnected Nanowire/Nanotube and Nanotube/Nanowire/Nanotube heterojunctions with branched topology," *Angewandte Chemie International Edition*, vol. 48, pp. 7166–7170, Sept. 2009.

[33] W. Cheng, M. Steinhart, U. Gösele, and R. B. Wehrspohn, "Tree-like alumina nanopores generated in a non-steady-state anodization," *J. Mater. Chem.*, vol. 17, no. 33, pp. 3493–3495, 2007.

[34] A. Y. Y. Ho, H. Gao, Y. C. Lam, and I. Rodríguez, "Controlled fabrication of multi-tiered three dimensional nanostructures in porous alumina," *Advanced Functional Materials*, vol. 18, pp. 2057–2063, July 2008.

[35] R. Zakeri, C. Watts, H. Wang, and P. Kohli, "Synthesis and characterization of nonlinear nanopores in alumina films," *Chem. Mater.*, vol. 19, no. 8, pp. 1954–1963, 2007.

[36] H. Asoh, K. Nishio, M. Nakao, T. Tamamura, and H. Masuda, "Conditions for fabrication of ideally ordered anodic porous alumina using pretextured al," *Journal of The Electrochemical Society*, vol. 148, no. 4, pp. B152–B156, 2001.

[37] B. Yan, H. T. M. Pham, Y. Ma, Y. Zhuang, and P. M. Sarro, "Fabrication of in situ ultrathin anodic aluminum oxide layers for nanostructuring on silicon substrate," *Applied Physics Letters*, vol. 91, pp. 053117–053117–3, Aug. 2007.

[38] T. Xu, G. Zangari, and R. M. Metzger, "Periodic holes with 10 nm diameter produced by grazing ar+ milling of the barrier layer in hexagonally ordered nanoporous alumina," *Nano Lett.*, vol. 2, no. 1, pp. 37–41, 2001.

[39] J. Liang, H. Chik, A. Yin, and J. Xu, "Two-dimensional lateral superlattices of nanostructures: Nonlithographic formation by anodic membrane template," *Journal of Applied Physics*, vol. 91, pp. 2544–2546, Feb. 2002.

[40] C. Y. Han, G. A. Willing, Z. Xiao, and H. H. Wang, "Control of the anodic aluminum oxide barrier layer opening process by wet chemical etching," *Langmuir*, vol. 23, no. 3, pp. 1564–1568, 2006.

[41] G. E. Thompson and G. C. Wood, "Porous anodic film formation on aluminium," *, Published online: 19 March 1981; | doi:10.1038/290230a0*, vol. 290, pp. 230–232, Mar. 1981.

[42] B. Marquardt, L. Eude, M. Gowtham, G. Cho, H. J. Jeong, M. Châtelet, C. S. Cojocaru, B. S. Kim, and D. Pribat, "Density control of electrodeposited ni nanoparticles/nanowires inside porous anodic alumina templates by an exponential anodization voltage decrease," *Nanotechnology*, vol. 19, p. 405607, Oct. 2008.

Chapter 2

Electrodeposition in PAA

This chapter presents the different advantages and goals of electrodeposition with a global overview of what has been done in this domain hitherto. It also presents our attempts to deposit metallic catalyst in the bottom of PAA templates using this technique, next step towards the fabrication of nanostructure-based field effect transistor. The ideal result would be to get a PAA with pores homogeneously filled, that is with no empty pore and no big catalyst size dispersion. Furthermore, these catalyst nanoparticles would be as small as possible, in order to ensure a quick and efficient growth (see chapter 3).

2.1 Introduction and brief state of the art

The control of the fabrication of PAA templates with desired geometry is a first essential step on the path of ordered, closely-packed 1D nanostructures synthesis. More generally, template-based nanostructures synthesis have been widely studied for the two past decades, and various synthesis methods have been developed with the aim of using these nanostructures in nanodevices. We can discern the electrodeposition and the electroless method. The latter gathers several different techniques, such as enforced infiltration of nanoparticles [1], high-pressure liquid or gas injection [2], [3], spontaneous reduction of dissolved salts [4], pore walls functionalization [5], [6], [7], chemical polymerization [8], sol-gel deposition [9] or chemical vapor deposition [10]. All these techniques are well reviewed by Hulteen and Martin [11]. In most of these cases the growth starts from the pore walls, and goes inwardly, which lead to nanotubules formation for short growths, and to nanofibers for longer growths.

Known for more than two centuries, the electrodeposition process was firstly used for electroplating, that is the coating of a conductive material with metal, from a solution containing the corresponding ionic form of the metal to be deposited. This simple process has been widely applied more recently to deposit various metals inside porous structures, thus leading to metallic nanowire arrays that are of high interest for various applications (especially in magnetic data storage devices [12], [13], [14]), to the deposit of catalytic particles for subsequent NW or NT organized growth [15], [16] [17], [18], but also to more specific applications (e.g. readout mechanisms [19]). Among the different methods used

to electrodeposit mater inside porous templates, research teams use either DC, AC or pulsed electrodeposition.

DC electrodeposition allows good control over crystallinity [20], [21], as well as good control over the composition along the NW [22], [14], but suffers from an inhomogeneous pore filling because of possible fluctuations in the alumina barrier layer thickness [23], leading to a different resistance in each pore. However, one can circumvent this problem either by using commercial through-hole polymeric porous membranes [20], [24], or by removing the barrier layer of the PAA membrane, but both options involves an additional metal deposition (sputtering or evaporation) step to finally perform the electrodeposition. Besides, in the case of PAA, a transfer of the alumina membrane -which therefore has to be relatively thick- is required [25], which is complex and not desirable for high scale fabrication.

AC electrodeposition has the advantage to get rid with the problem created by the alumina barrier layer, that acts as the dielectric of a capacitor. Caboni was the first one to develop this method to fill nanopores [26]. During the cathodic half-cycles (negative voltage), metal ions are reduced at the bottom of the pores, and the rectifying behaviour of the alumina ("valve metal oxide") prevents the reoxidation during the anodic half-cycles [27]. Moreover, these anodic half-cycles allow the capacitor to discharge, and thus the electrolyte to keep a metal ion concentration high enough to keep on providing the cathode for reduction. These advantages can give a good pore filling, which is more difficult to get under DC conditions [28], [29], [30]. However, this technique suffers from a bad control over the structure of the deposited material [31],

According to Nielsch et al., pulsed electrodeposition (PED) can also provide a good and homogeneous pore filling [23]. Instead of AC deposition, they used a short constant current cathodic pulse to reduce the metallic ions, immediately followed by an even shorter anodic pulse in order to discharge the capacitor (barrier layer). They also added a "delay time", quite longer, so as the electrolyte recovers its concentration homogeneity near the electrolyte/deposited metal interface. This method has been successfully followed by many groups ever since [32], [33], [34].

All methods taken together, a very wide variety of metals has been successfully deposited at the bottom of vertical pores. Let's mention gold [5], [35], [25], copper [36], [37], [21], nickel [38], [23], [28], [39], cobalt [40], [38], [32], [41], iron [27], but also silver [42], ruthenium [24], palladium [33], [4]... Even semiconducting materials have been deposited: CdS [43], CdSe and CdTe [44], Bi_2Te_3 [45], CuS [46]. Cao and Liu grouped together these results in their review [47], mentioning also conductive polymers and oxides deposition, of a lesser interest for our work.

In our case, the electrodeposition has been used as a convenient mean to deposit catalytic particles at the bottom of the pores, with a view to growing nanostructures inside the PAA. To emphasize the versatility of the PAA as a template, several kinds of metallic catalysts have been successfully deposited in this way, leading to silicon nanowires as well as carbon nanotubes confined growth.

2.2 The principles of electrodeposition

Basically, an electrodeposition is always based on the same set-up. Two electrodes are required, the sample to be coated being chosen as the cathode, where the reduction of cations will take place. The cations can be supplied in two different ways: either the anode is made of the solid form of the material one want to deposit on the cathode, or the cations are already dissolved in a conductive electrolyte. In the first case the anode is therefore oxidized to dissolve metallic cations inside the electrolyte, in the other case the cations usually come from the dissolution of salts, and the anode is a neutral electrode (platinum, graphite...) that doesn't react with the electrolyte. Both electrodes are dipped inside the electrolyte, and connected to a power supply. When an appropriate voltage is applied between the two electrodes, metallic ions surrounding the cathode are reduced onto the surface of the cathode with the following reaction: $\mathrm{M}^{z+}_{(aq)} + \mathrm{ze}^- -> \mathrm{M}_{(s)}$, creating a thin deposit of the element M on it. The longer the process, the thicker the deposited layer; this process is commonly called "electroplating" and is widely used in the industry. The electric field helps the cations to reach the surface of the cathode and to ensure a sufficient cationic concentration around the sample (cathode) for the reaction to go on. Not any applied potential can lead the reduction reaction. Indeed, both oxidation of the metal and reduction of the cations occur, and the applied voltage determines which one prevails. They actually exactly compensate for a particular potential, called the Nernst potential, defined as

$$E_{Nernst} = \frac{RT}{zF} ln \left(\frac{a_{M^{z+}}}{a_M} \right)$$

where

- R is the universal gas constant,
- T is the absolute temperature,
- z is the number of electrons involved in the reaction,
- F is the Faraday constant,
- $a_{M^{z+}}$ and a_M are the chemical activities of the cation and the non-oxidized metal, respectively.

Thus, to ensure a deposition, the applied potential has to be superior to the Nernst potential. We talk about an overpotential. In order to realize a proper electrodeposition, the three-electrode system is widely used. It involves the same two electrodes mentioned above, namely an anode and a cathode, and an additional electrode, called the reference electrode (RE). In the following we will talk about working electrode (WE) for the cathode, and counter electrode (CE) for the anode. The reference electrode acts as an electrochemical half-cell itself, since it contains both oxidant and reductant of a redox couple. Its role is to provide a well-known and constant potential, from which the working electrode potential will be based. Indeed, the potential of the counter electrode is constantly adjusting to balance the excess or the lack of charge induced by the working electrode, and therefore cannot be used as a reference. The reference electrode is able to measure the potential of the working electrode, but also to control and adjust it. Besides,

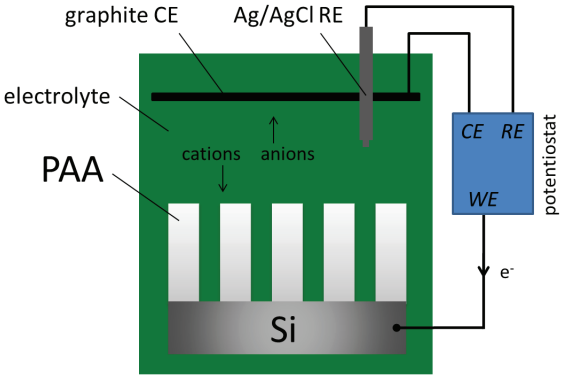

Figure 2.1: Drawing of the three-electrode system used for electrodeposition. WE, CE and RE stand for working, counter and reference electrode, respectively.

these measurements don't interfere with the global process, since the reference electrode doesn't pass any current. On the contrary, the counter electrode passes all the current, and thus provides electrons to the circuit for the reduction at the working electrode.

2.3 Experiments, results and discussion

2.3.1 The experimental setup

For the reasons brought up in the previous paragraph, we used a three-electrode system in order to control efficiently the deposition of nanoparticles at the bottom of the PAA (Figure 2.1). Contrary to the anodization case, here the sample plays the role of the cathode, where reduction takes place. It is called the working electrode in this particular set-up and is mounted on the same sample holder as for the anodization step. The anode, or counter electrode, is the same graphite electrode as the one used in the anodization set-up ('a' in Figure 1.3(c)) and the reference electrode is an Ag/AgCl electrode, whose potential is 0.21 V compared to the standard hydrogen electrode (SHE). Contrary to classical electroplating set-ups, the anode doesn't need to be the same material as the material to be deposited, since the desired cations have already been inserted during the making of the electrolyte. This set-up was supplied by a potentiostat from *Bio-Logic*, controlled via the software EC-Lab from the same company, which allows to design easily any wave to be applied on the working electrode. Thus we have been able to test several deposition modes mentioned in the introduction of this chapter. The potentiostatic mode (i.e. the measurement of current as a function of a desired voltage) is more relevant than the galvanostatic mode, since the former allows to apply the overpotential that can lead the diffusion-limited current, which is easy to control. On the contrary, the galvanostatic mode will impose a current that, if higher than the diffusion-limited current, will not necessarily supply the overpotential needed for the reduction of the species. As a reference structure for studying the electrodeposition process inside PAA, we used the same process for fabricating the PAA templates as described in chapter 1. Most

often the anodization has been performed completely, that is until the Al layer is totally consumed and transformed into porous alumina, in order to free ourselves from the problem caused by the barrier layer. As the electrolytes behave differently depending on their composition, several species have been studied, namely copper (Cu), nickel (Ni) and gold (Au). This has also been done with the view to being able to grow different nanostructures in the PAA, since the latter cannot grow with any catalyst (see chapter 3).

2.3.2 The pulsed electrodeposition (PED) parameters study

In order to grow SiNWs, several catalysts are available. Among them, Cu and Au appear to be promising candidates since they catalyse SiNW growth (see chapter 3), but also because their deposition inside PAA is a widely spread process (2.1). As for CNT growth, Ni was chosen to catalyse their growth, and the work achieved by our team about Ni electrodeposition [48] was chosen as a basis to study Cu and Au deposition.

Electrolytes composition and chemical reactions

The electrolyte used for the Cu electrodeposition was made from solid $CuSO_4$,$5H_2O$ dissolved in deionised water. 250 g.L^{-1} are necessary to get a Cu^{2+} concentration of 1 mol.L^{-1} (1 M). The pH of the solution was set to low values ($\approx$ 3.4) by adding 50 g.L^{-1} of boric acid (H_3BO_3) in the solution, in order to ensure a good conductivity of the electrolyte.

Ni electrolyte has been prepared from a classical recipe called "Watts bath", containing $NiSO_4$,$6H_2O$ (300 g.L^{-1}), $NiCl_2$,$6H_2O$ (50 g.L^{-1}) and H_3BO_3 (50 g.L^{-1}) dissolved in deionized water. The as-prepared solution has a Ni^{2+} concentration of 1.35 mol.L^{-1}.

As for the solution used for Au electrodeposition, we dissolved 0.93 g.L^{-1} of $HAuCl_4$,$3H_2O$ and 30 g.L^{-1} of H_3BO_3 in deionized water. $HAuCl_4$ dissociates into H^+ and $AuCl_4^-$, which is the oxidant of the redox couple $AuCl_4^-/Au$. The concentration of $AuCl_4^-$ ions in the solution is therefore $\approx 2.36.10^{-3}$ mol.L^{-1}.

In the following table are gathered the three metals that we chose to study, with their corresponding redox couples, redox processes, and standard potentials.

Metal	Redox couple	Standard reduction potential (E°)	Reaction
Cu	Cu^{2+}/Cu	+ 0.34	$Cu^{2+} + 2e^- \rightarrow Cu$
Ni	Ni^{2+}/Ni	- 0.25	$Ni^{2+} + 2e^- \rightarrow Ni$
Au	$AuCl_4^-/Au$	+ 1.0	$AuCl_4^- + 3e^- \rightarrow Au + 4\ Cl^-$

Table 2.1: Standard reduction potential are given with respect to the SHE.

The applied signal

Figure 2.2 shows a drawing of a single sweep that is applied a certain number of times during an electrodeposition experiment. It consists in a short (a few milliseconds) negative voltage, applied between the WE and the RE, immediately followed by a longer

period (most often 90 ms) at the open circuit potential (OCP). The OCP is the potential that exists naturally between the WE and the RE without applying any potential in the cell, and thus corresponds to the "zero" with respect to the chemical potentials existing in the electrolyte. In other words, the OCP is the potential applied at the WE for which no current passes in through the CE.

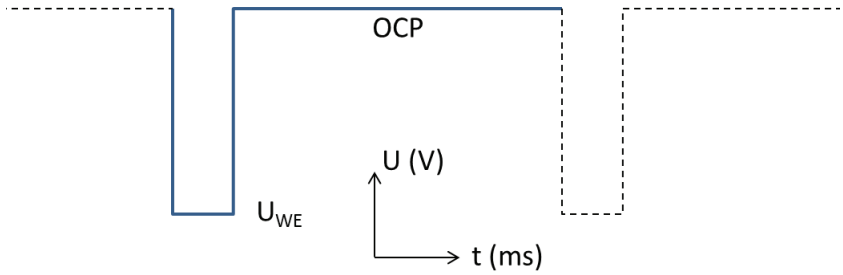

Figure 2.2: Drawing of a pulse used for pulsed electrodeposition experiments. OCP = Open Circuit Potential.

For some reasons, the maximum current may slightly change during the electrodeposition process, or between one experiment to another. It is therefore more relevant to compare the effective global charge involved in the redox reaction, i.e the reductive charge and the oxidative charge. These values are directly given by the software that drives the electrodeposition, simply using this relation:

$$Q = \int_{t_i}^{t_f} I(t)\,\mathrm{d}t$$

Figure 2.3(a) shows a magnified part of a typical I(t) curve, obtained from a Ni electrodeposition experiment. We notice that the current passing between the WE and the CE behaves like in a capacitor that charges and discharges alternatively. Figure 2.3(b) shows both the applied voltage and the current response for one particular pulse. Graphically we estimate this capacitor as being charged or discharged ≈ 1 ms after the applied potential change.

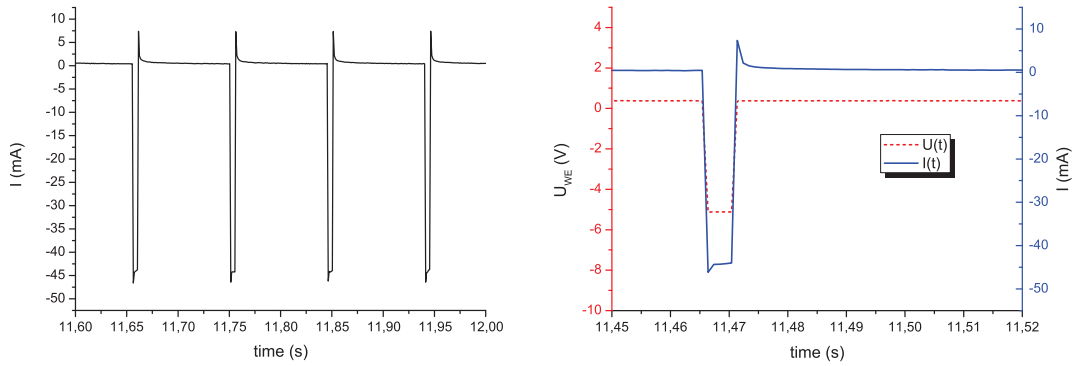

(a) (b)

Figure 2.3: (a) Example of an I(t) curve (only four pulses out of 500 are represented) from a Ni electrodeposition experiment. (b) is a magnified view of one pulse from (a), with the superimposed voltage signal (doted red line).

Study of some electrodeposition parameters

The following study has been made only with Cu and Ni deposition, the Au deposition being performed later on during the thesis. A lot of parameters have been varied to understand which ones of them could lead to a proper deposition of Cu at the bottom of the pores.

First of all, the influence of the number of sweeps is very intuitive to understand. A sweep has to be understood as explained in Figure 2.2, that is the voltage pulse followed by the resting time. Of course the more sweeps applied the more material is deposited. Here we just give an example to illustrate the difference between a PAA after 50 sweeps and a PAA after 200 sweeps of pulsed electrodeposition of Cu. As can be seen on Figure 2.4, Cu particles are much longer after 200 sweeps, due to the higher number of cathodic pulses, that leads to a higher total charge reduced at the bottom of the pores. The software automatically gives the value of this charge at the end of the deposition: the 50-sweep deposition corresponds to a 47.6 mC charge, and the 200-sweep deposition to a 167 mC charge. We notice the equivalence between the number of sweeps and the cathodic charge (exchanged charge during the cathodic pulses), since four times as many sweeps leads to approximately a four times bigger charge. This long deposition can be useful for fabricating long metallic nanowires, as illustrated in Figure 2.5(a), where a large amount of Ni nanowires is visible, liberated from their PAA template after a 3000-sweep deposition. The corresponding cathodic charge was 1.48 C, and the maximum length has been evaluated to $\approx$ 750 nm, inside a PAA 950 nm thick. But a too long process can lead to an over-deposition. Indeed, when a Ni nanowire reaches the top of the template, the deposition is not confined in the pore anymore. Therefore, as this kind of growth is electro-chemical, the deposition occurs where the resistivity is the lowest, i.e on all the surface of the protruding nanowires, which leads to the formation of a metallic

layer over the porous template, as illustrated in Figure 2.5(b). This picture corresponds to a 6000-sweep Ni electrodeposition, with a cathodic charge of 2.36 C.

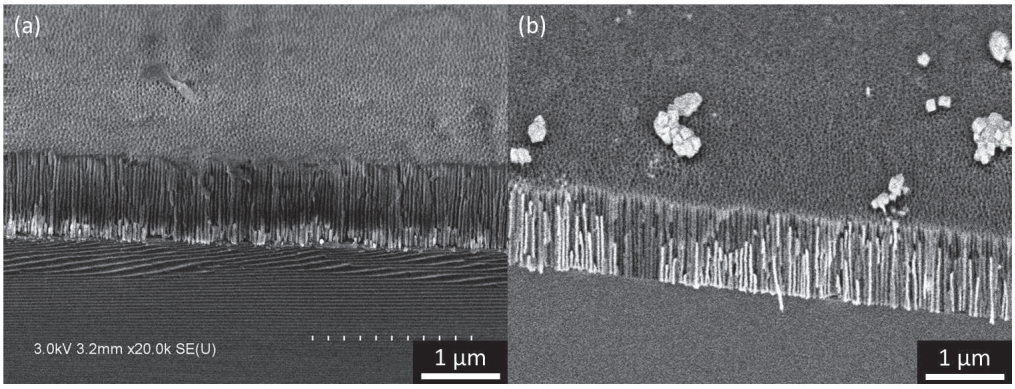

Figure 2.4: SEM cross-sections of PAA templates after Cu electrodeposition at -8.5 V. (a) 50 sweeps and (b) 200 sweeps.

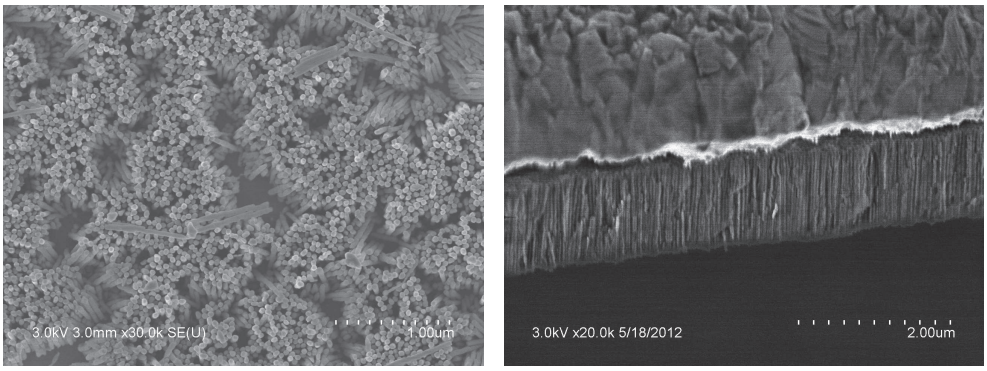

(a) (b)

Figure 2.5: (a) SEM top-view of liberated Ni nanowires, after the PAA has been etched away with chromic acid. (b) SEM cross-section of a PAA after a 6000-sweep Ni deposition (the massive overdeposited Ni is clearly visible onto the template).

As already mentioned in p.35, the voltage applied between the working electrode and the reference electrode has to be carefully chosen in such a way that it is high enough after the various voltage drops caused by a barrier layer, by the resistance of the electrolyte, by the electrode itself, but also by the Si substrate. To determine which voltage to use for a given set-up (i.e a given PAA, on a given substrate, dipped inside a given electrolyte), one can perform a voltamperometry experiment, which consists in measuring the current response between the WE and the CE when submitted to a sweeping voltage (applied between the WE and the RE). If the applied voltage is too low to overcome the whole serial resistance detailed above, a very low current passes because the final voltage available to reduce the cations is not high enough. When the voltage reaches the

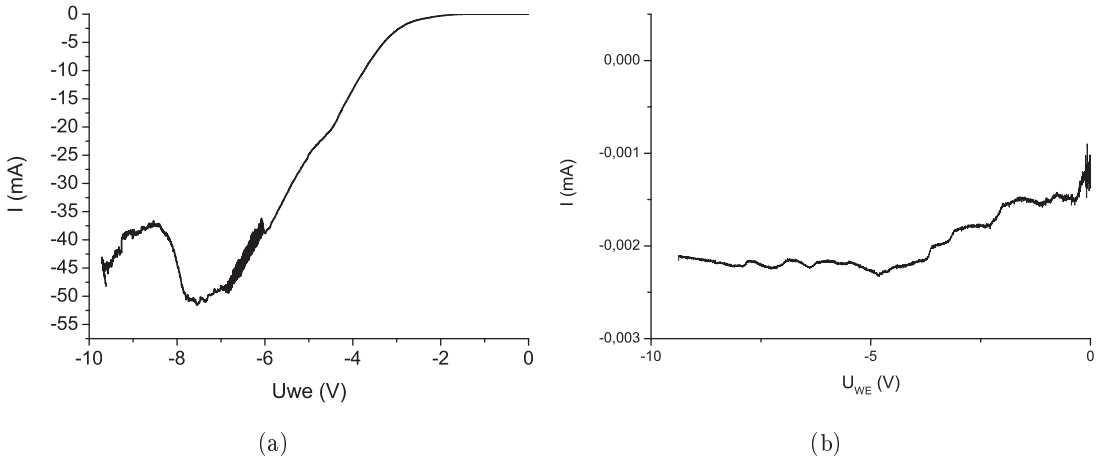

(a) (b)

Figure 2.6: Current between WE and CE as a function of a sweeping voltage (U_{we}) applied between WE and RE, for a Ni electrodeposition experiment. The silicon substrate resistivity are (a) $\rho < 0.005$ Ω.cm. (b) $\rho =$ 1-10 Ω.cm.

overpotential value, the current starts to increase because cations begin to be reduced, and the higher the voltage the higher the current. As an illustration, we used the Linear Sweep Voltage (LSV) tool of EC-Lab in order to determine the voltage threshold from which the current starts to increase. In a typical porous template anodized in sulfuric acid, we deposited Ni with a voltage decreasing from 0 V to -10 V with a rate which has been set to 100 mV/s. The corresponding I(V) curve is visible in Figure 2.6(a), and the threshold voltage has thus been estimated to -1.8 V in this specific configuration. However, a too high voltage could provoke hydrogen evolution in the electrolyte, which could inhibit the electrodeposition [23]. We noticed some instabilities from ≈ -6.0 V, and an abrupt current increase occurred from -8 V, without being able to explain it. We therefore performed the same LSV experiment, but stopping the sweeping before these instabilities, i.e from 0 V to -6 V. However we didn't detect any difference in terms of filling, both PAA exhibiting a high overfilling of Ni with a thick Ni layer on the top of the surface of the PAA. Note that the resistivity of the silicon substrate used in this experiment was very low: $\rho < 0.005$ Ω.cm. In the case of a higher resistivity ($\rho =$ 1-10 Ω.cm), the only current we were able to detect in the [-10 V ; 0 V] range was in the order of a nA (Figure 2.6(b)), electrodeposition was therefore impossible in this condition.

We also studied the influence of the cathodic pulse duration, i.e the time during which the cations can be reduced. For these experiments, Ni was chosen as the metal to deposit at the bottom of the pores. The duration of the cathodic part of the pulse was varied from 1 ms to 20 ms, and the resting time was kept constant in every case (90 ms). As can be seen on the top left picture of Figure 2.7, one millisecond was not sufficient to deposit any particle inside the pores. It is most probably due to a too short total reduction time (500 x 1 ms = 500 ms of active pulse), as proved by Figure 2.7 (top-right), which shows the

same PAA after 2500 one-millisecond pulses. In this sample the total reduction time is 5 times longer (2500 milliseconds), and one can finally see some particles at the bottom of the pores. For 5 ms pulses, one can see some small particles at the bottom of the pores (up to 120 nm), but a large number of pores are still empty. Doubling the cathodic time led to larger Ni particles (up to 330 nm), but also to a large size dispersion. It is supposed that a longer cathodic time can allow other nucleation sites to appear, while "older" particles keep on growing, thus leading to a wide size dispersion. We performed the same experiment with a longer cathodic time (20 ms), but surprisingly we couldn't find a big increase of the particle size. The taller particles were even the same size as for 10 ms pulses, except there were more long particles, and less small ones.

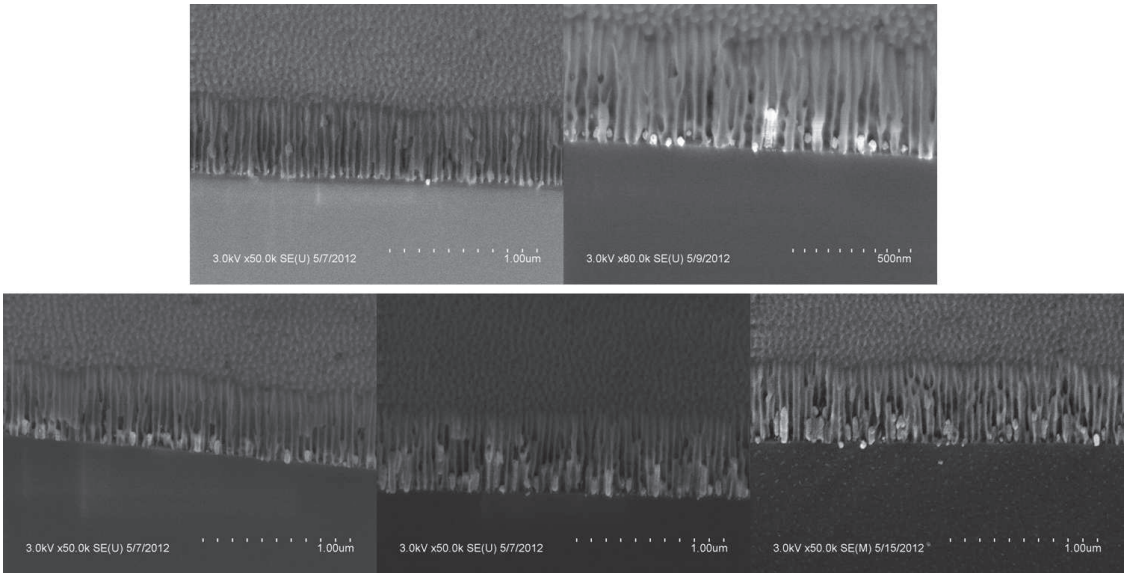

Figure 2.7: SEM cross-sections of PAA after Ni electrodeposition. Top: 1 ms pulses, 500 sweeps and 2500 sweeps, respectively. Bottom: 5 ms, 10 ms and 20 ms pulses, respectively (500 sweeps).

This may be understood considering the notion of the total reducing time. If we have a look on the I(t) curve of the experiment performed with 5 ms pulses, we can see that the maximum current is almost constant from the first pulse to the last one (around -40 mA, see Figure 2.8). The same statement can be made for the 10 ms pulses, but we notice that for 100 ms pulses, the maximum current significantly decreases from -36 mA in the very first pulse, down to -12.5 mA in the last pulse. The reduction seems therefore to be less efficient for longer cathodic pulses, regardless of the number of pulses.

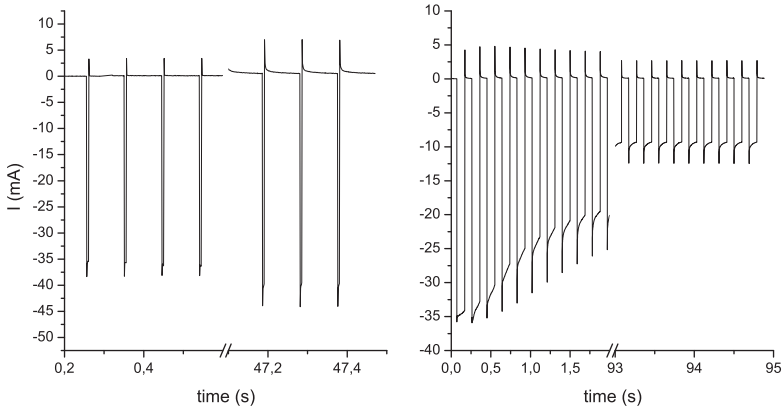

Figure 2.8: I(t) curves showing the first and the last pulses of (left) 5 ms pulses experiment and (right) 100 ms experiment.

This is confirmed by the 2500 one-millisecond pulses experiment mentioned earlier, which shows a maximum current almost constant ($\approx$ -40 mA) despite the high number of pulses because the corresponding total time is low (2500 x 1 ms = 2500 ms). Nevertheless, according to this theory, we should have observed a decreasing maximum current from a certain time in the 20 ms experiment, for example. But it was barely the case. An assumption can be that a too long pulse leads to a faster decrease of the maximum current because the resting time is not long enough to discharge the capacity mentioned in p.38. Indeed, in the 100 ms pulses experiment, the maximum current starts to decrease as soon as the second pulse, which is contradictory with the constant maximum current observed in the 5 ms pulses experiment. The same experiment has been done with 300 ms resting time between each pulse, leading to the exact same result as with 90 ms resting time. Further investigations are therefore required to understand the phenomenon that makes the reducing current decrease for long pulse duration, for example studying the pulse time / resting time ratio, or inserting an anodic pulse between the cathodic pulse and the resting time. However that may be, it is more reliable to use short pulse times, like 5 or 10 ms if one wants to foresee the evolution of the reducing current. As a complement we plotted the equivalent charge obtained from the I(t) curve for the different pulse times mentioned above (Figure 2.9). It shows that the relation between the charge and the duration of the cathodic pulse is not linear, thus confirming that it's getting harder to reduce cations if voltage pulses are too long.

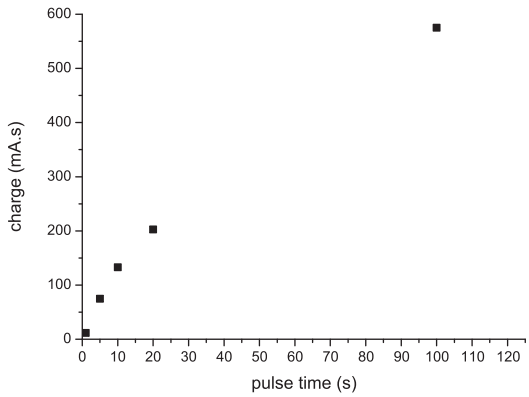

Figure 2.9: Equivalent charge (obtained integrating I(t) curves) as a function of pulse duration.

Finally, we found that the maximum current (reached during the voltage pulses) was always comprised between -25 and -40 mA, which is consistent with the value predicted by the LSV experiment for a -5.5 V potential (Figure 2.6(a)). Note that even for the 100 ms pulse experiment, the very first pulses were also around -35 mA. No special study has been done about Au electrodeposition, but an illustration is shown in Figure 2.10, which has been realized under the same conditions as for optimized Ni deposition, that is -5.5 V, 5 ms pulses, except only 50 sweeps were applied. We note the same problem of inhomogeneity in size, and a filling a bit less than 50 %. In summary, the fact that several metals have been successfully deposited opens the way towards the growth of several kinds of nanostructures, and can provide different options for the same nanostructure.

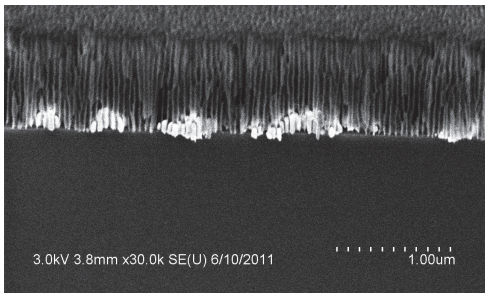

Figure 2.10: SEM cross-section of a PAA after Au electrodeposition. Fifty 5 ms pulses were applied, at -5.5 V.

The cross-sections of filled PAA are a fast and convenient way to get a global idea of the filling efficiency, but it is more relevant to compare top views of samples which PAA templates have been removed from. With this point of view, the height of the particles are no longer comparable, but the estimation of their distribution over the sample and the density is far better. The next section deals with the way we observed the density of catalyst nanoparticles from the top.

2.3.3 Liberating the nanoparticles with PAA etching

The PAA can be removed in several ways, always using wet etching in order to get an isotropic reaction. The solution made of chromic trioxide and phosphoric acid (CrO_3 + H_3PO_4) used between the first and the second anodization (p.16) is often used for this purpose, but H_3PO_4 alone or NaOH is also used. However, these solutions may have a bad impact on the nanoparticles once the PAA is completely etched. We have noticed that even for long etching times in CrO_3/H_3PO_4 solution, i.e prolonged far after the PAA dissolution, the Au particles looked intact, with no evidence of a chemical attack, but that Cu and Ni seem affected by such an etching. We assume that the presence of the ion CrO_3^-, which is know to be a powerful oxidant, can be responsible of the degradation of the Cu and Ni particles, and therefore to dissolve the NWs inside the solution if they are exposed for a long time in the etching solution. We therefore tried NaOH as an etchant, which is actually commonly used for this purpose [36], [29], [21]. A 1 M NaOH solution was found to efficiently etch PAA with an etching rate quite higher than the CrO_3/H_3PO_4 solution, which is beneficial for the metallic particles in the pores. However, the etching time has to be controlled, since a chemical reaction also occurs between the particles and NaOH. An illustration is given with Cu nanowires in Figure 2.11. We see that the PAA is completely removed after an etching as short as 1 minute (Figure 2.11(a)), but that a longer etching leads to the degradation of the NWs, that then form piles of small particles (Figure 2.11(c)). It is supposed that the reaction taking place is:

$$Cu^{2+} + 2\,OH^- \longrightarrow Cu(OH)_2$$

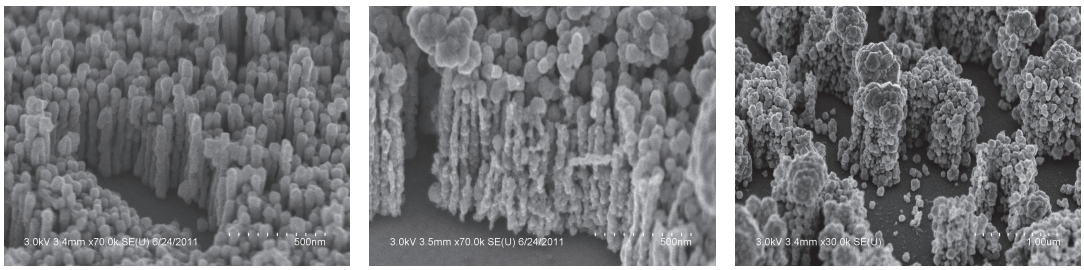

(a) (b) (c)

Figure 2.11: Evolution of the aspect of Cu NWs after PAA removal with 1 M NaOH. Samples have been immersed for (a) 1 min, (b) 5 min and (c) 20 min.

Interestingly, the Au particles haven't been subjected to any damage, as illustrated in Figure 2.12, where a sample which has been immersed into a 2 M NaOH solution for 18 min is shown. We see that the Au particles are still intact, smooth and straight, thanks to the noble nature of gold.

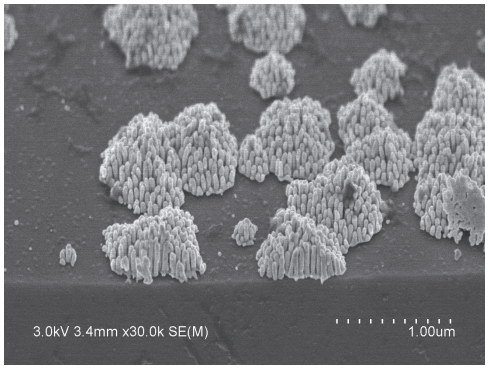

Figure 2.12: SEM picture of liberated Au particles after PAA removal with 2 M NaOH for 18 min.

2.3.4 Water plasma treatment for a better filling with catalysts

We thought that a bad wetting of the electrolyte in some pores of the PAA could be the cause of the inhomogeneous filling observed in some sample. The reason why some pores would be less adamant to receive the liquid than others is not really understood, but a global treatment has been planned anyway in order to improve the hydrophilicity of the walls of the pores. Several ways have been investigated in the literature in that purpose, like UV exposure [49], [50], [51], hydrophilic molecules grafting [52], plasma treatments [53], [54], [55]... Some publications have shown that the hydrophilicity of numerous different surfaces could be increased, by exposing them to a water plasma for a few minutes [53]. According to the latter article, the water contact angles have noticeably decreased after this treatment, leading to a better arrangement of polystyrene beads on these surfaces. The authors used Fourier transfer infrared (FTIR) spectroscopy to show that this better hydrophilicity was due to the high number of hydroxyl groups on the surface, produced with the water plasma treatment. We therefore attempted to expose our samples to such a plasma, hoping the creation of hydroxyl groups on the pore walls that could improve the wetting of the electrolyte during the electrodeposition process. We thus expect to get a more homogeneous filling of the pores with the catalysts.

The plasma reactor and the experimental conditions

To do so, we used a plasma chamber, usually dedicated to graphene or CNT growth, with a triode configuration. The plasma is generated between two electrodes (the anode and the grid on Figure 2.13) that allow to create a high density plasma, whose species can then be extracted towards the sample mounted onto a third electrode, negatively charged, called the cathode on Figure 2.13. This configuration has the advantage to generate the glow discharge and to create the plasma separately, which avoids unstable phenomena to occur on the sample, but also to control precisely the flow and the energy of the active species on the sample, by biasing it with an independent voltage. We proceeded as follows: the PAA sample was mounted directly on the cathode with the

help of two ceramic rods, and locked inside the plasma chamber. Water vapour (10 sccm) was injected via the gas inlet until the pressure reaches 1.5 mbar in the chamber. At this moment, the plasma was generated by applying a discharge of 700 V between the anode and the grid, remaining the cathode unplugged. Such a high voltage was necessary to ignite the plasma, but the voltage was quickly decreased down to 500 V, in order to limit sparkles and flashes events. The generation of the plasma always leads to a pressure increase, and the voltage was adjusted to stabilize it at 2.0 mbar. Once the plasma is stable (no sparkle or pressure variation), the cathode is plugged in order to extract a downstream plasma towards the sample, and the diffusion current, that is the current created by the extracted species, is set as a variable parameter whose influence on the sample was studied, as well as the exposure time.

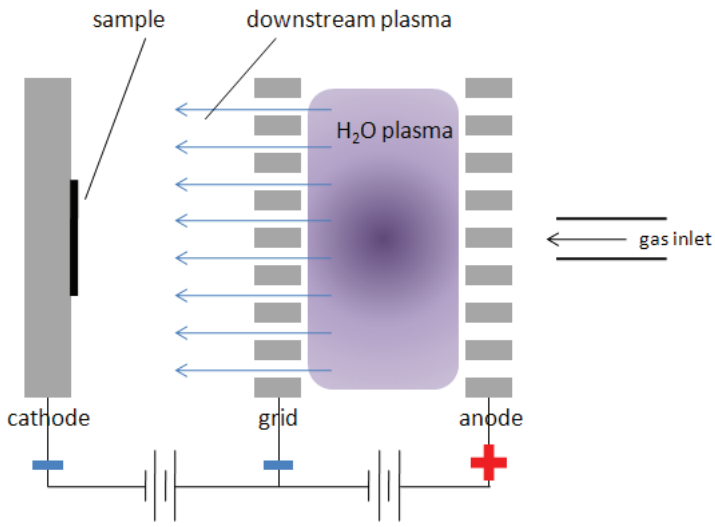

Figure 2.13: Drawing of the plasma chamber with the triode configuration.

Results

The pore filling

The samples used to explore the influence of water plasma on the filling of catalyst were PAA templates with open pores, fabricated as described in 1.3.2. It is capital to check whether all the pores are correctly opened, so as the presence of a barrier layer doesn't interfere with the potential influence of the plasma treatment. As a first attempt, we performed a 15 min water plasma exposure to a part of a 1.2 µm-thick PAA template. A copper electrodeposition was performed successively on the non-treated part and on the treated part of this sample, with 50 pulses of 5 ms at -8.5 V. Each pulse was separated by a 90 ms resting time. By observing the cross-sections of these samples with the SEM, we discovered in the treated sample some large zones (several microns in length) with a high density of Cu particles at the bottom of the pores that we couldn't find in

the non-treated sample. As shown of Figure 2.14, these zones exhibit longer particles, and gather more neighbouring particles than in the non-treated sample. Some particles reach more than 700 nm in length, and a filled-pore area could even spread over 15 µm (Figure 2.14(c)), which couldn't be found at all in the non-treated sample. The plasma treatment seems therefore to impact the electrodeposition process, leading to greater filled zones, and to taller particles. However, though the filling seems easier, it appears quite inhomogeneous and still reveals high disparities, in terms of particles height and of density over the sample.

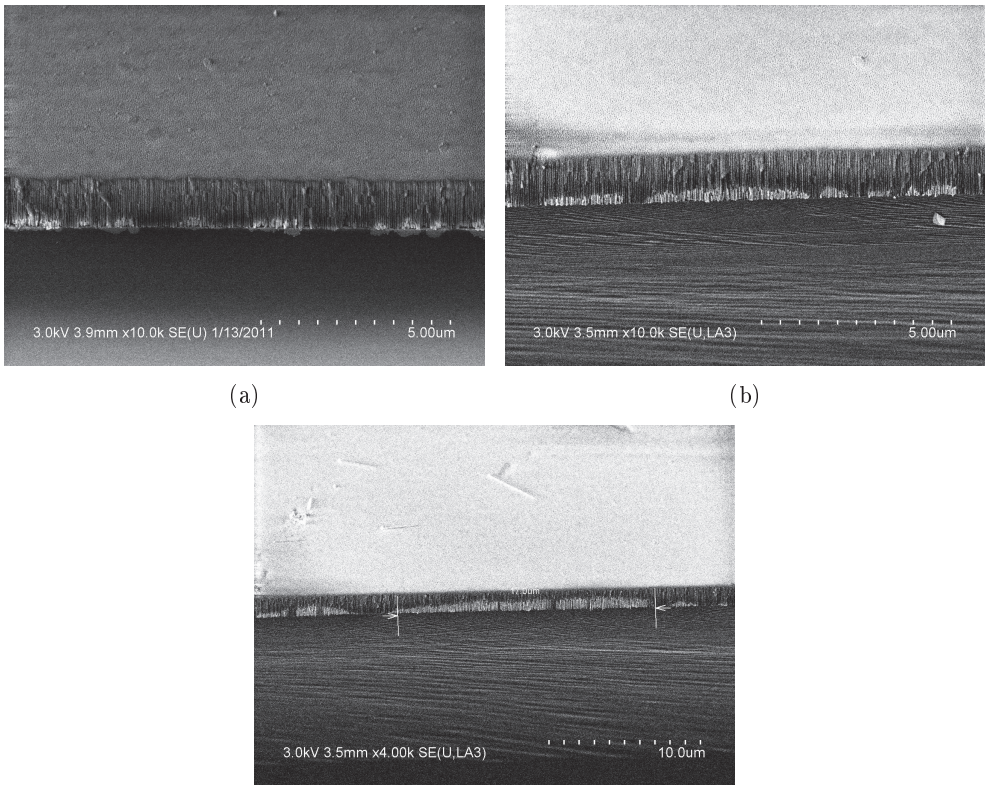

(a) (b)

(c)

Figure 2.14: Cross-sections of (a) non-treated and (b) and (c) water plasma-treated (for 15 min) PAA after Cu electrodeposition. (c) shows a large zone of 17 µm with a quasi 100% pore filling.

In order to detect a potential influence of the exposure time, a similar experiment has been carried out with a total exposure time of 40 min, on a sample prepared in the same conditions. More pulses (100) have been applied in order to deposit more Cu, especially in the non-treated sample where the lack of particles was problematic to conclude firmly about the influence of the plasma. The shape of the pulse (5 ms followed by a 90 ms resting time) and the voltage (-8.5 V) were kept the same as before. Here again a clear increase of the number of pores filled with Cu is noted for the treated sample, as well as

a better height homogeneity (Figure 2.15). The Cu particles often almost reach the top of the membrane (Figure 2.15(c)), which is not the case in the non-treated sample. It has been noticed that large zones with neighbouring filled pores were more frequent than on the sample exposed to the water plasma for 15 min, which may indicate a greater impact of the plasma for a longer exposure.

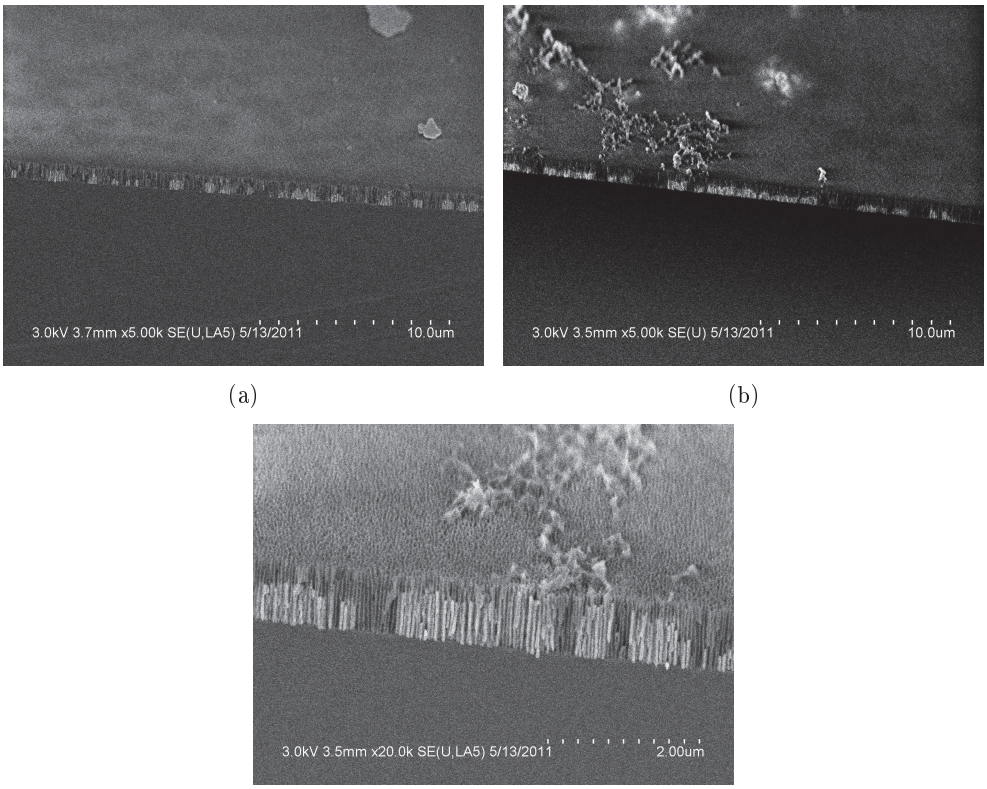

(a) (b)

(c)

Figure 2.15: Cross-sections of (a) non-treated and (b) and (c) water plasma-treated (for 40 min) PAA after Cu electrodeposition.

We used a NaOH solution to chemically etch the PAA membranes of the latter samples, in order to reveal all the Cu particles deposited on the Si substrate. The corresponding top views with different scales are visible in Figure 2.16 and Figure 2.17. This comparison allows to notice a clear higher density of Cu nanoparticles on the sample that has been treated with the water plasma, which is attributed to a better hydrophilicity of the pore walls.

In order to validate this assumption in a general way, we wanted to realize similar experiments with other materials. We wanted to know whether Ni or Au electrodeposition could be also affected by a preliminary plasma treatment of the PAA host.

We have seen earlier that Ni was generally easier to deposit than Cu or Au in our membranes and already shows high density of pore filling. The density of Ni particles

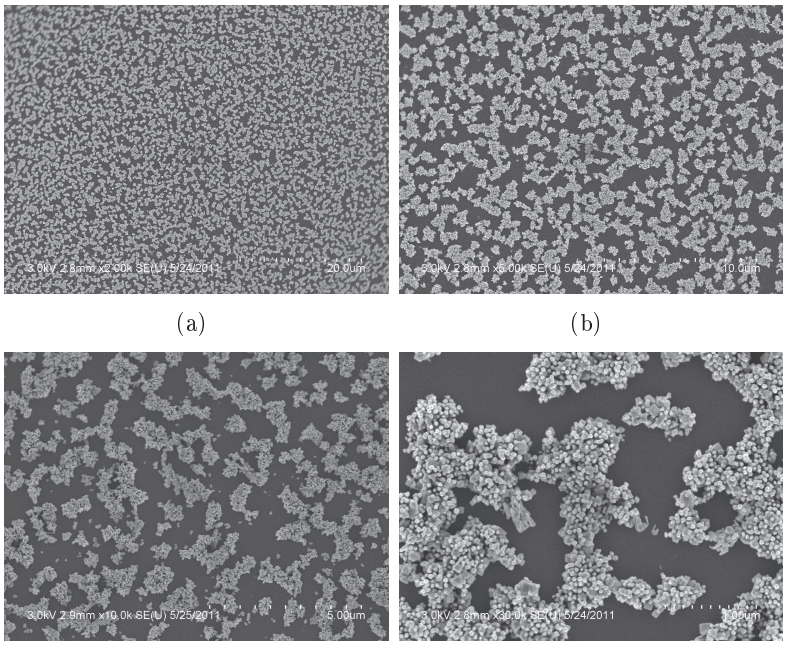

Figure 2.16: Top views of non-treated samples after Cu electrodeposition and PAA removal with NaOH. The magnification increases from 2000x to 30000x from (a) to (d).

was thus not expected to be much improved and we verified that no noticeable difference was visible between a top view SEM picture of a plasma-treated sample with the PAA removed and of a non-treated one. Nevertheless, some tilted views revealed an interesting improvement in terms of height homogeneity. In this experiment we used the optimized parameters of Ni electrodeposition described in 2.3.2, with 500 pulses of 5 ms at -5.5 V. In the case of a non-treated sample, a lot of Ni particles are visible on the PAA-removed sample, but their size differ slightly, some of them looking like small balls and other like small wires (see Figure 2.18(a)). On the contrary, if the PAA is exposed to a 40 min water plasma before the Ni electrodeposition, the size of the Ni particles is dramatically increased (for a same voltage and number of pulses) up to 200 nm in length, but overall their size is quite less dispersed (see Figure 2.18(b) and 2.18(c)). Therefore, in the case of Ni, no effect could be shown in terms of density improvement, but the water plasma treatment seems to have an effect upon the electrodeposition process since it influences a lot the size and the size distribution of the deposited particles.

As for Au deposition, surprising results have been found. Indeed, without being able to explain why, we found that the pore filling was worse after the plasma treatment than in non-treated PAAs (Figure 2.19).

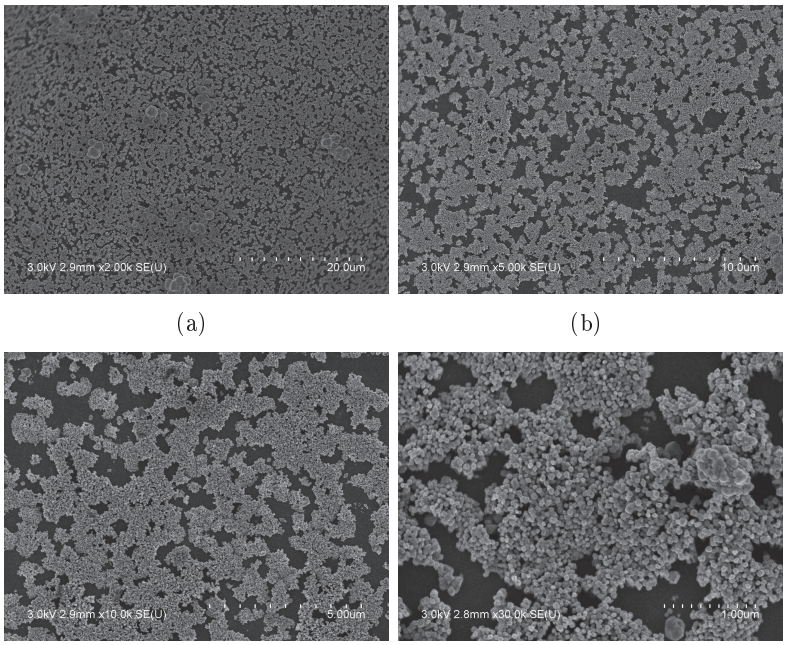

(a) (b)

(c) (d)

Figure 2.17: Top views of water plasma-treated (40 min) samples after Cu electrodeposition and PAA removal with NaOH. The magnification increases from 2000x to 30000x from (a) to (d), for an easy comparison with Figure 2.16.

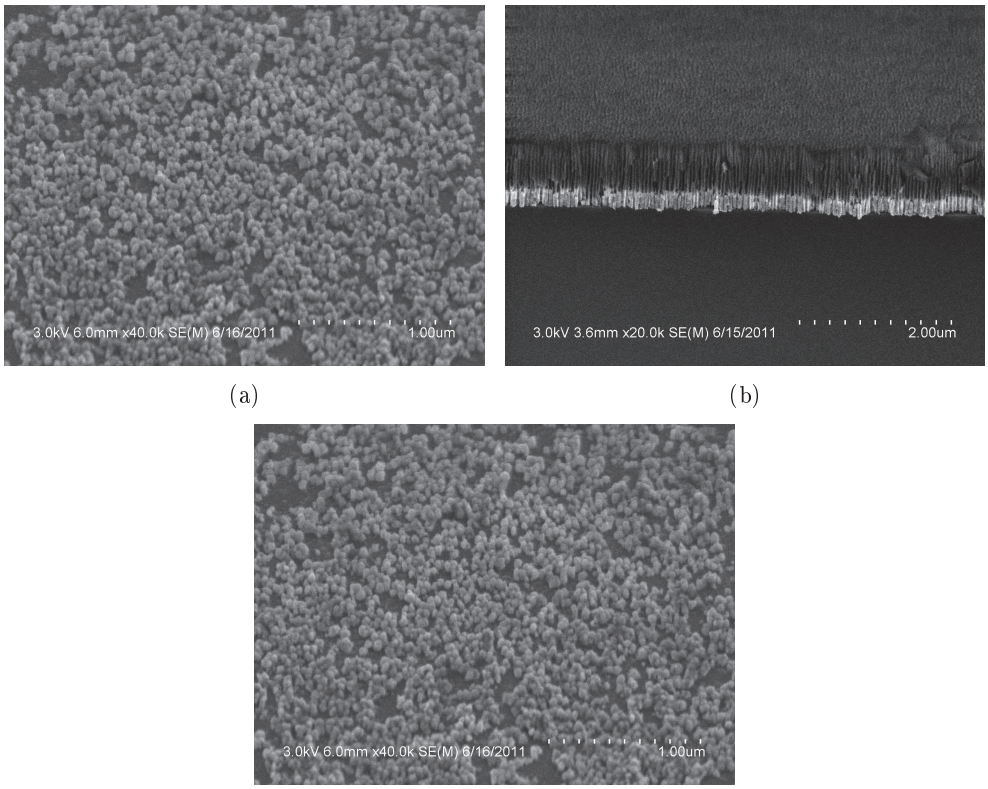

Figure 2.18: Tilted views of (a) non-treated and (b), (c) water plasma-treated samples after Ni electrodeposition. PAA has been removed with NaOH in (a) and (c).

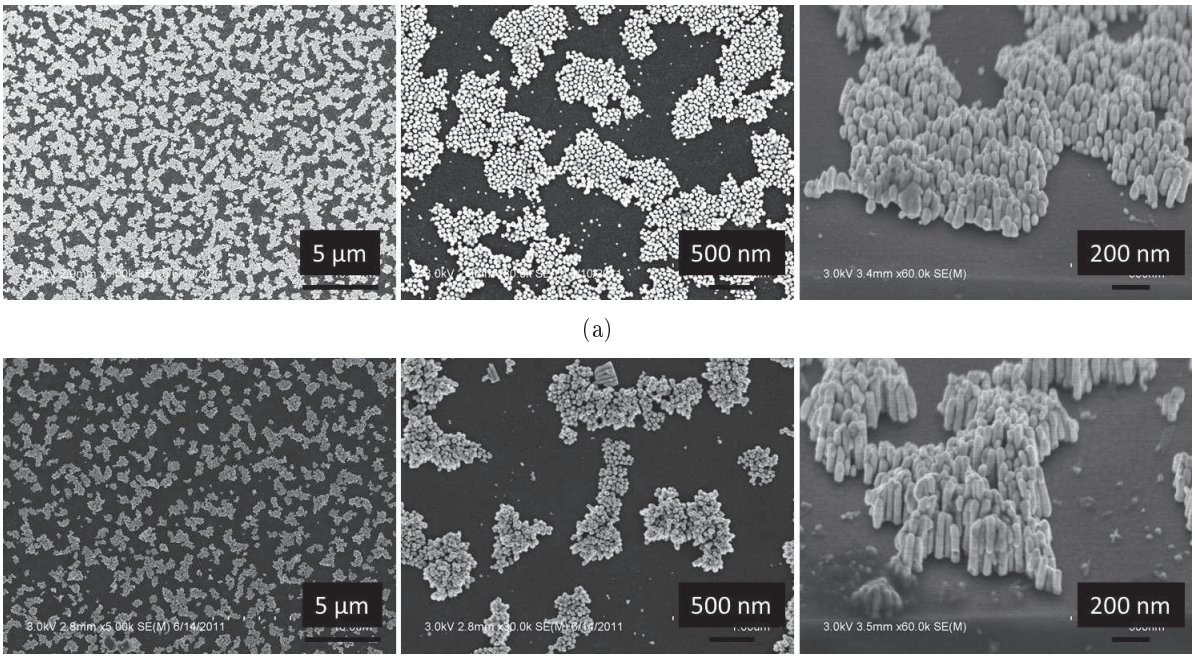

Figure 2.19: (a) non-treated and (b) plasma-treated sample after Au electrodeposition.

Contact angle measurements

In order to support the assumption that the PAA becomes more hydrophilic thanks to the H_2O plasma, a basic study about contact angles has been carried out. Shortly after the plasma treatment (i.e no more than one day) that lasted 40 min, the contact angle between the PAA surface and a droplet of water has been measured and compared to a droplet deposited on a non-treated PAA. It turned out that the droplet spread much more on the treated PAA surface, exhibiting a contact angle as low as about 20° (Figure 2.20(a)), while the same droplet is repelled from the non-treated PAA, which has a hydrophobic surface (contact angle about 110°, see Figure 2.20(b)). The same experiment has been performed on many samples that had been treated long before the angle measurement (several weeks), and no difference has been noticed with a non-treated sample. All the droplets exhibited a high contact angle (about 110°), as if no treatment has been done on the samples.

These results show that the plasma does modify the hydrophilicity properties of the PAA, and that liquid solution is more likely to penetrate inside the pores after a water plasma treatment. However, the effect provided by the plasma treatment has a limited life span, that could be estimated by doing some systematic measurements after the plasma exposure. The effect lasts at least several hours up to one day, since the exposure of the sample shown in Figure 2.20(a) has been done the day before the contact angle measurement.

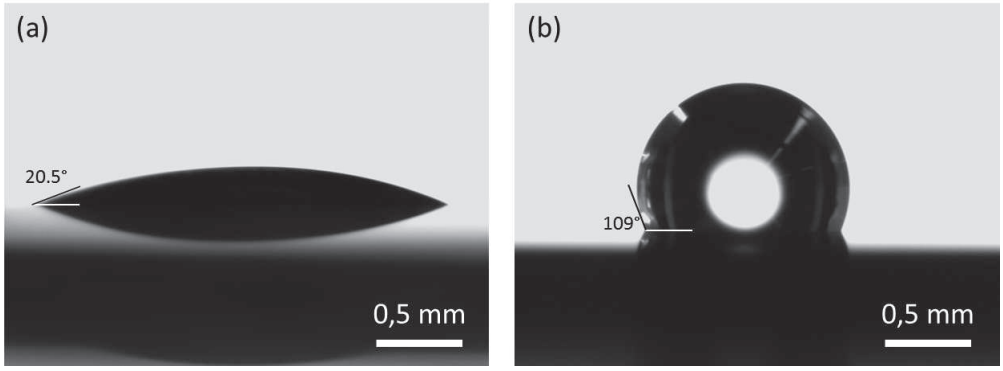

Figure 2.20: Pictures of a droplet of water on the surface of (a) a plasma-treated PAA (40 min) and (b) a non-treated PAA.

Generally speaking, the idea of treating the PAA template with a water plasma looks promising, but would deserve to be investigated more thoroughly since no strong general trend has been drawn, despite the interesting results presented here. Indeed, some evidence of the influence of the plasma on the pore filling with catalyst particles have been highlighted, but some problems such as lack of reproducibility and apparently contradictory results (Au deposition) still remain. Nevertheless this method could definitely be an interesting and elegant method to improve the homogeneity of the catalyst particles, by modifying the hydrophilicity of the PAA.

2.4 Conclusion

This chapter sums up several methods reported in the literature to deposit nanoparticles inside porous templates. One of them, the pulsed electrodeposition, has been studied here. We varied the main parameters of the pulses (length, number, magnitude...) and studied their influence on the aspect of the electrodeposited particles and the filling efficiency. We made this study using Cu, Ni and Au solutions, and each metal has been successfully deposited at the bottom of the pores of a PAA template. We managed to control their size by adjusting the applied voltage, the pulse duration, as well as the number of pulses of a deposition process. Optimized conditions for each metal have been set, which is promising regarding a subsequent growth of nanostructures inside PAA, since both SiNW (from Cu or Au) and CNT (from Ni) growths are thus potentially feasible from these metals. The conditions that led to the best results in terms of control and homogeneity of metal catalyst deposition will be used as a basis to grow 1D nanostructures in PAA and more complex porous structures.

Nevertheless, even if pore filling efficiency has been considerably improved, our investigations didn't allow to reach an ideal 100 % filling, except with Ni. The development of an original method, based on a plasma treatment of the PAA template, has been started and revealed promising results concerning the pore filling and should be investigated

more thoroughly.

The results obtained from chapter 1 and chapter 2 pave the way towards a capital part of this thesis: the confined growth of one-dimensional nanostructures, which will be the subject of the next chapter.

Bibliography

[1] M. R. Lukatskaya, L. A. Trusov, A. A. Eliseev, A. V. Lukashin, M. Jansen, P. E. Kazin, and K. S. Napolskii, "Controlled way to prepare quasi-1D nanostructures with complex chemical composition in porous anodic alumina," *Chemical Communications*, vol. 47, no. 8, p. 2396, 2011.

[2] Z. Zhang, J. Y. Ying, and M. S. Dresselhaus, "Bismuth quantum-wire arrays fabricated by a vacuum melting and pressure injection process," *Journal of Materials Research*, vol. 13, no. 07, pp. 1745–1748, 1998.

[3] N. R. B. Coleman, M. A. Morris, T. R. Spalding, and J. D. Holmes, "The formation of dimensionally ordered silicon nanowires within mesoporous silica," *J. Am. Chem. Soc.*, vol. 123, no. 1, pp. 187–188, 2000.

[4] Q. Xu, G. Meng, X. Wu, Q. Wei, M. Kong, X. Zhu, and Z. Chu, "A generic approach to desired metallic nanowires inside native porous alumina template via redox reaction," *Chem. Mater.*, vol. 21, no. 12, pp. 2397–2402, 2009.

[5] V. P. Menon and C. R. Martin, "Fabrication and evaluation of nanoelectrode ensembles," *Anal. Chem.*, vol. 67, no. 13, pp. 1920–1928, 1995.

[6] M. De Leo, F. C. Pereira, L. M. Moretto, P. Scopece, S. Polizzi, and P. Ugo, "Towards a better understanding of gold electroless deposition in track-etched templates," *Chem. Mater.*, vol. 19, no. 24, pp. 5955–5964, 2007.

[7] C. m. Yang, H. s. Sheu, and K. j. Chao, "Templated synthesis and structural study of densely packed metal nanostructures in MCM41 and MCM48," *Advanced Functional Materials*, vol. 12, pp. 143–148, Feb. 2002.

[8] R. V. Parthasarathy, K. L. N. Phani, and C. R. Martin, "Template synthesis of graphitic nanotubules*," *Advanced Materials*, vol. 7, pp. 896–897, Nov. 1995.

[9] B. B. Lakshmi, P. K. Dorhout, and C. R. Martin, "SolGel template synthesis of semiconductor nanostructures," *Chem. Mater.*, vol. 9, no. 3, pp. 857–862, 1997.

[10] T. Kyotani, L.-f. Tsai, and A. Tomita, "Preparation of ultrafine carbon tubes in nanochannels of an anodic aluminum oxide film," *Chem. Mater.*, vol. 8, no. 8, pp. 2109–2113, 1996.

[11] J. C. Hulteen and C. R. Martin, "A general template-based method for the preparation ofnanomaterials," *Journal of Materials Chemistry*, vol. 7, pp. 1075–1087, Jan. 1997.

[12] S. Y. Chou, M. S. Wei, P. R. Krauss, and P. B. Fischer, "Single domain magnetic pillar array of 35 nm diameter and 65 gbits/in2 density for ultrahigh density quantum magnetic storage," *Journal of Applied Physics*, vol. 76, pp. 6673 –6675, Nov. 1994.

[13] L. Gravier, S. Serrano-Guisan, and J.-P. Ansermet, "Spin-dependent peltier effect in Co/Cu multilayer nanowires," *Journal of Applied Physics*, vol. 97, no. 10, p. 10C501, 2005.

[14] F. de Menten de Horne, L. Piraux, and S. Michotte, "Fabrication and physical properties of Pb/Cu multilayered superconducting nanowires," *Applied Physics Letters*, vol. 86, pp. 152510–152510–3, Apr. 2005.

[15] K.-K. Lew and J. M. Redwing, "Growth characteristics of silicon nanowires synthesized by vapor-liquid-solid growth in nanoporous alumina templates," *Journal of Crystal Growth*, vol. 254, pp. 14–22, June 2003.

[16] X. y. Zhang, L. d. Zhang, G. w. Meng, G. h. Li, N. y. JinPhillipp, and F. Phillipp, "Synthesis of ordered single crystal silicon nanowire arrays," *Advanced Materials*, vol. 13, pp. 1238–1241, Aug. 2001.

[17] J. Li, C. Papadopoulos, J. M. Xu, and M. Moskovits, "Highly-ordered carbon nanotube arrays for electronics applications," *Applied Physics Letters*, vol. 75, pp. 367–369, July 1999.

[18] T. Hashishin, Y. Tono, and J. Tamaki, "Guide growth of carbon nanotube arrays using anodic porous alumina with ni catalyst," *Japanese Journal of Applied Physics*, vol. 45, pp. 333–337, 2006.

[19] S. R. Nicewarner-Pena, "Submicrometer metallic barcodes," *Science*, vol. 294, pp. 137–141, Oct. 2001.

[20] M. E. T. Molares, V. Buschmann, D. Dobrev, R. Neumann, R. Scholz, I. U. Schuchert, and J. Vetter, "SingleCrystalline copper nanowires produced by electrochemical deposition in polymeric ion track membranes," *Advanced Materials*, vol. 13, pp. 62–65, Jan. 2001.

[21] T. Gao, G. Meng, J. Zhang, Y. Wang, C. Liang, J. Fan, and L. Zhang, "Template synthesis of single-crystal cu nanowire arrays by electrodeposition," *Applied Physics A: Materials Science & Processing*, vol. 73, no. 2, pp. 251–254, 2001.

[22] J.-G. Wang, M.-L. Tian, T. E. Mallouk, and M. H. W. Chan, "Microstructure and interdiffusion of template-synthesized Au/Sn/Au junction nanowires," *Nano Lett.*, vol. 4, no. 7, pp. 1313–1318, 2004.

[23] K. Nielsch, F. Müller, A. P. Li, and U. Gösele, "Uniform nickel deposition into ordered alumina pores by pulsed electrodeposition," *Advanced Materials*, vol. 12, pp. 582–586, Apr. 2000.

[24] M. Tian, J. Wang, J. Kurtz, T. E. Mallouk, and M. H. W. Chan, "Electrochemical growth of single crystal metal nanowires via a two dimensional nucleation and growth mechanism," *Nano Lett.*, vol. 3, no. 7, pp. 919–923, 2003.

[25] X. Y. Zhang, L. D. Zhang, Y. Lei, L. X. Zhao, and Y. Q. Mao, "Fabrication and characterization of highly ordered au nanowire arrays," *Journal of Materials Chemistry*, vol. 11, pp. 1732–1734, Jan. 2001.

[26] V. Caboni, 1936.

[27] D. AlMawlawi, N. Coombs, and M. Moskovits, "Magnetic properties of fe deposited into anodic aluminum oxide pores as a function of particle size," *Journal of Applied Physics*, vol. 70, pp. 4421–4425, Oct. 1991.

[28] A. J. Yin, J. Li, W. Jian, A. J. Bennett, and J. M. Xu, "Fabrication of highly ordered metallic nanowire arrays by electrodeposition," *Applied Physics Letters*, vol. 79, pp. 1039–1041, Aug. 2001.

[29] G. A. Gelves, Z. T. M. Murakami, M. J. Krantz, and J. A. Haber, "Multigram synthesis of copper nanowires using ac electrodeposition into porous aluminium oxide templates," *Journal of Materials Chemistry*, vol. 16, pp. 3075–3083, July 2006.

[30] A. Jagminas, A. Jagminiene, and E. Matulionis, "Uniformity of ac growth of copper nanowires within the porous alumina template from acidic Cu(II) sulphate solutions," 2003.

[31] N. J. Gerein and J. A. Haber, "Effect of ac electrodeposition conditions on the growth of high aspect ratio copper nanowires in porous aluminum oxide templates," *J. Phys. Chem. B*, vol. 109, no. 37, pp. 17372–17385, 2005.

[32] G. P. Sklar, K. Paramguru, M. Misra, and J. C. LaCombe, "Pulsed electrodeposition into AAO templates for CVD growth of carbon nanotube arrays," *Nanotechnology*, vol. 16, pp. 1265–1271, Aug. 2005.

[33] K. Kim, M. Kim, and S. M. Cho, "Pulsed electrodeposition of palladium nanowire arrays using AAO template," *Materials Chemistry and Physics*, vol. 96, pp. 278–282, Apr. 2006.

[34] X. Huang, L. Li, X. Luo, X. Zhu, and G. Li, "Orientation-controlled synthesis and ferromagnetism of single crystalline co nanowire arrays," *Journal of Physical Chemistry C*, vol. 112, pp. 1468–1472, 2008.

[35] M. Wirtz and C. R. Martin, "TemplateFabricated gold nanowires and nanotubes," *Advanced Materials*, vol. 15, pp. 455–458, Mar. 2003.

[36] R. Inguanta, S. Piazza, and C. Sunseri, "Influence of the electrical parameters on the fabrication of copper nanowires into anodic alumina templates," *Applied Surface Science*, vol. 255, pp. 8816–8823, Aug. 2009.

[37] S. Shingubara, O. Okino, Y. Sayama, H. Sakaue, and T. Takahagi, "Two-dimensional nanowire array formation on si substrate using self-organized nanoholes of anodically oxidized aluminum," *Solid-State Electronics*, vol. 43, pp. 1143–1146, June 1999.

[38] H. Zeng, M. Zheng, R. Skomski, D. Sellmyer, Y. Liu, L. Menon, and S. Bandyopadhyay, "Magnetic properties of self-assembled co nanowires of varying length and diameter," *David Sellmyer Publications*, May 2000.

[39] B. Marquardt, L. Eude, M. Gowtham, G. Cho, H. J. Jeong, M. Châtelet, C. S. Cojocaru, B. S. Kim, and D. Pribat, "Density control of electrodeposited ni nanoparticles/nanowires inside porous anodic alumina templates by an exponential anodization voltage decrease," *Nanotechnology*, vol. 19, p. 405607, Oct. 2008.

[40] M. Sun, G. Zangari, M. Shamsuzzoha, and R. M. Metzger, "Electrodeposition of highly uniform magnetic nanoparticle arrays in ordered alumite," *Applied Physics Letters*, vol. 78, pp. 2964–2966, May 2001.

[41] G. J. Strijkers, J. H. J. Dalderop, M. A. A. Broeksteeg, H. J. M. Swagten, and W. J. M. de Jonge, "Structure and magnetization of arrays of electrodeposited co wires in anodic alumina," *Journal of Applied Physics*, vol. 86, pp. 5141–5145, Nov. 1999.

[42] G. Sauer, G. Brehm, S. Schneider, K. Nielsch, R. B. Wehrspohn, J. Choi, H. Hofmeister, and U. Gösele, "Highly ordered monocrystalline silver nanowire arrays," *Journal of Applied Physics*, vol. 91, pp. 3243–3247, Mar. 2002.

[43] S. Mondal, A. Dhar, and S. Ray, "Optical properties of CdS nanowires prepared by dc electrochemical deposition in porous alumina template," *Materials Science in Semiconductor Processing*, vol. 10, pp. 185–193, Aug. 2007.

[44] J. D. Klein, R. D. Herrick, D. Palmer, M. J. Sailor, C. J. Brumlik, and C. R. Martin, "Electrochemical fabrication of cadmium chalcogenide microdiode arrays," *Chem. Mater.*, vol. 5, no. 7, pp. 902–904, 1993.

[45] M. S. Sander, R. Gronsky, T. Sands, and A. M. Stacy, "Structure of bismuth telluride nanowire arrays fabricated by electrodeposition into porous anodic alumina templates," *Chem. Mater.*, vol. 15, no. 1, pp. 335–339, 2002.

[46] K. V. Singh, A. A. Martinez-Morales, K. N. Bozhilov, and M. Ozkan, "A simple way of synthesizing single-crystalline semiconducting copper sulfide nanorods by using ultrasonication during template-assisted electrodeposition," *Chem. Mater.*, vol. 19, no. 10, pp. 2446–2454, 2007.

[47] G. Cao and D. Liu, "Template-based synthesis of nanorod, nanowire, and nanotube arrays," *Advances in Colloid and Interface Science*, vol. 136, pp. 45–64, Jan. 2008.

[48] B. Marquardt, "Organisation nanometrique de composant (nanotubes de carbone) utilisant des membranes verticales d'alumine anodique poreuse." http://tel.archives-ouvertes.fr/index.php?halsid=pjkpepq00t6oqf5pbns4tj48j3&view_this_doc=pastel-00005877&version=1, Dec. 2009.

[49] M. Takeuchi, Y. Onozaki, Y. Matsumura, H. Uchida, and T. Kuji, "Photoinduced hydrophilicity of TiO2 thin film modified by ar ion beam irradiation," *Nuclear Instruments and Methods in Physics Research Section B: Beam Interactions with Materials and Atoms*, vol. 206, pp. 259–263, May 2003.

[50] M. Nyström and P. Järvinen, "Modification of polysulfone ultrafiltration membranes with UV irradiation and hydrophilicity increasing agents," *Journal of Membrane Science*, vol. 60, no. 2–3, pp. 275–296, 1987.

[51] H.-Y. Chou, E.-K. Lee, J.-W. You, and S.-S. Yu, "Photo-induced hydrophilicity of TiO2xNx thin films on PET plates," *Thin Solid Films*, vol. 516, pp. 189–192, Dec. 2007.

[52] F. Liu, B.-K. Zhu, and Y.-Y. Xu, "Improving the hydrophilicity of poly(vinylidene fluoride) porous membranes by electron beam initiated surface grafting of AA/SSS binary monomers," *Applied Surface Science*, vol. 253, pp. 2096–2101, Dec. 2006.

[53] Y. Jong-Bin, K. Nam-Hoon, and L. Hyun-Yong, "Universal surface hydrophilicity obtained by using low-temperature plasma H_2O gas for nanosphere lithography," *Journal of the Korean Physical Society*, vol. 58, p. 1, Jan. 2011.

[54] K. N. Pandiyaraj and V. Selvarajan, "Non-thermal plasma treatment for hydrophilicity improvement of grey cotton fabrics," *Journal of Materials Processing Technology*, vol. 199, pp. 130–139, Apr. 2008.

[55] J. Lai, B. Sunderland, J. Xue, S. Yan, W. Zhao, M. Folkard, B. D. Michael, and Y. Wang, "Study on hydrophilicity of polymer surfaces improved by plasma treatment," *Applied Surface Science*, vol. 252, pp. 3375–3379, Mar. 2006.